LASING ACTION AND SUPERCONTINUUM GENERATION IN NANO- AND MICRO-STRUCTURES

A THESIS

SUBMITTED TO THE PROGRAM OF MATERIALS SCIENCE AND

NANOTECHNOLOGY

AND THE INSTITUTE OF ENGINEERING AND SCIENCE

OF BILKENT UNIVERSITY

IN PARTIAL FULFILLMENT OF THE REQUIREMENTS

FOR THE DEGREE OF

MASTER OF SCIENCE

By

Duygu Akbulut

January, 2009

I certify that I have read this thesis and that in my opinion it is fully adequate, in scope and in quality, as a thesis for the degree of Master of Science.

Assist. Prof. Dr. Mehmet Bayındır(Supervisor)

I certify that I have read this thesis and that in my opinion it is fully adequate, in scope and in quality, as a thesis for the degree of Master of Science.

Assoc. Prof. Dr. Ceyhun Bulutay

I certify that I have read this thesis and that in my opinion it is fully adequate, in scope and in quality, as a thesis for the degree of Master of Science.

Res. Assist. Prof. Dr. Aykutlu Dâna

Approved for the Institute of Engineering and Sciences:

Prof. Dr. Mehmet Baray
Director of Institute of Engineering and Sciences

ABSTRACT

LASING ACTION AND SUPERCONTINUUM GENERATION IN NANO- AND MICRO-STRUCTURES

Duygu Akbulut
M.S. in Materials Science and Nanotechnology
Supervisor: Assist. Prof. Dr. Mehmet Bayındır
January, 2009

Supercontinuum generation is the substantial broadening of electromagnetic radiation due to nonlinear interactions with the transporting medium. It finds application in a wide range of areas, including spectroscopy, frequency metrology, optical coherence tomography and telecommunications.

Whispering gallery mode microresonators confine light in a micron scale area via total internal reflection mechanism. Among these structures, microtoroid is especially interesting since it combines ultrahigh quality factor and chip integrability. Applications of such structures include nonlinear and quantum optics, biological and chemical sensing, telecommunications and quantum electrodynamics.

In the first part of the present work, continuum generation from a nanostructured chalcogenide glass (As_2Se_3) core, high temperature polymer (polyethersulfone, PES) cladding fiber was experimentally investigated. Simulation results for nonlinear interactions inside a microtoroid are also provided. In the second part, polymer coated toroidal microresonators were employed for observation of laser

action. Owing to high quantum efficiency of the polymer, the observed lasing threshold has a very low value of 200 pJ/pulse despite free space excitation.

Keywords: nonlinear optics, supercontinuum generation, chalcogenide glasses, toroidal microcavities, π-conjugated polymers, laser action

ÖZET

NANO VE MİKRO YAPILARDA LAZER ETKİSİ VE GENİŞ BANTLI IŞIK ÜRETİLMESİ

Duygu Akbulut
Malzeme Bilimi ve Nanoteknoloji, Yüksek Lisans
Tez Yöneticisi: Yar. Doç. Dr. Mehmet Bayındır
Ocak, 2009

Geniş bantlı ışık üretimi elektromanyetik dalganın, içerisinde ilerlediği ortamla lineer olmayan etkileşimleri sonucunda gözlenen önemli miktardaki spektral genişleme olarak tanımlanır. Spektroskopi, frekans metrolojisi, optik koherans tomografisi ve telekomünikasyon alanlarında uygulaması vardır.

Fısıldayan galeri modlu mikrorezonatörlerde ışık toplam iç yansıma mekanizmasıyla mikron boyutlarında alanlara hapsedilir. Bu yapılar içinde mikrotoroid, çok yüksek kalite faktörleri ve çipe entegre edilebilirlik özellikleri açısından ilgi uyandırıcıdır. Bu yapıların uygulama alanları arasında ise lineer olmayan optik ve kuantum optiği, biyolojik ve kimyasal algılama, telekomünikasyon ve kuantum elektrodinamiği vardır.

Tezin ilk kısmında chalcogenide (As_2Se_3) öz ve PES koruyucu bölgeden oluşan nanoyapılı bir fiberde geniş bantlı ışık üretimi incelenmiştir. Ayrıca mikrotoroid içindeki lineer olmayan optik etkileşimleri için yapılmış FDTD simülasyon sonuçları da verilmiştir.

İkinci kısımda ise, polimer kaplanmış toroid mikrorezonatörler lazer etkisi gözlenmesi amacıyla kullanılmıştır. Polimerin yüksek kuantum verimi

sayesinde lazer etkisi serbest uzay uyarımı sayesinde 200 pJ/atım gibi düşük eşik değerlerinde gözlenebilmiştir.

Anahtar Kelimeler: lineer olmayan optik, geniş bantlı ışık üretimi, chalcogenide camlar, toroid mikrokovuklar, π-konjuge polimerler, lazer etkisi

ACKNOWLEDGMENTS

Firstly, I would like to thank my supervisor Mehmet Bayındır for his help and guidance throughout my master's period.

I also would like to thank Bayındır group members: Dr. Abdullah Tülek, Dr. Mecit Yaman, Dr. Hakan Deniz, Hülya Budunoğlu, Özlem Köylü, Özlem Şenlik, Adem Yıldırım, Mert Vural, Kemal Gürel, Esat Kondakçı, Yavuz N. Ertaş, Murat Kılınç, Erol Özgür, Ekin Özgür and Can Koral.

I would like to thank Dr. Abdullah Tülek again for teaching me fabrication and measurement techniques and guiding me whenever I needed help.

Also, I would like to thank technicians and engineers of Institute of Materials Science and Nanotechnology (UNAM) and Advanced Research Laboratory (ARL) for their help in technical issues whenever needed.

I wish to give my special thanks to my family for their patience, support and love. I specifically thank my mother, without her help, I would have had a hard time during the period leading to this thesis. I am also grateful to Engin, for his understanding, patience and support during the writing of this thesis.

Finally, we thank TUBITAK and TUBA for their financial support.

Contents

1 INTRODUCTION **1**

2 THEORETICAL BACKGROUND **4**

2.1 Nonlinear Optics 4

2.1.1 Optical Kerr Effect 5

2.1.2 Self Phase Modulation 6

2.1.3 Cross Phase Modulation 7

2.1.4 Four Wave Mixing 8

2.1.5 Stimulated Raman Scattering 9

2.1.6 Stimulated Brillouin Scattering 10

2.1.7 Pulse Propagation in Nonlinear Media 11

2.2 Laser Action 17

2.2.1 Absorption, Spontaneous Emission and Stimulated Emission 17

2.2.2 Superradiance, Superfluorescence, Amplified Spontaneous Emission 20

2.3 Whispering Gallery Mode Resonators 22

2.3.1 Optical Modes 22

2.3.2 Free Spectral Range 23

2.3.3 Finesse 24

2.3.4 Mode Volume 24

2.3.5 Quality Factor 24

2.3.6 Cavity Build-up Factor 25

3 CONTINUUM GENERATION in MICROSTRUCTURED CHALCOGENIDE OPTICAL FIBER and TOROIDAL MICRORESONATOR 26

3.1 Introduction 26

3.2 Description of The Fiber 30

3.3 Numerical Simulations for The Fiber 37

3.4 Experimental Setup 39

3.5 Measurements and Results 43

3.5.1 1500 nm central wavelength 44

3.5.2 At 2000 nm central wavelength 50

3.6 WGM Microresonators 57

3.7 FDTD Simulations for Nonlinear Effects on Toroidal Microresonator 58

4 LASING ACTION FROM POLYMER COATED TOROIDAL MICRORESONATOR 61

4.1 Introduction 61

4.2 π-Conjugated Polymers and DOO-PPV 62

4.3 Aim and Motivations 64

4.4 Microtoroid Fabrication 65

4.5 Experimental Setup 72

4.6 Measurements and Results 73

5 CONCLUSION and FUTURE WORKS 77

List of Figures

2.1 (a) Three-level laser system. (b) Four-level laser system. Adapted from Reference [36]. 20

2.2 Examples of different WGM microresonators: (a) microdisk, (b) microsphere, (c) microtoroid. Adapted from Reference [38]. 22

3.1 Comparison of different broadband sources. Adapted from Reference [45]. 27

3.2 The drawing steps of the nanostructured As_2Se_3 fiber. 31

3.3 The nanostructured chalcogenide fiber used in the experiments. . 32

3.4 The measured refractive index, extinction coefficient and the calculated material dispersion for As_2Se_3. 32

3.5 The measured refractive index and the extinction coefficient for PES. 33

3.6 (a) The fiber created in RSoft CAD Environment^{TM} for effective refractive index calculation. (b) The material refractive index profile of the nanostructured fiber calculated at 1.55 μm wavelength.(c) 3D image of the nanostructured fiber. 34

3.7 The total chromatic dispersion of the nanostructured fiber compared to the material dispersion of As_2Se_3. 35

3.8 Optical microscope image of the fiber after polishing by hand using polishing films. 36

3.9 (a) SEM image of the fiber after being cleaved and flattened by microtome. (b) SEM image of the fiber's core area after being polished by FIB. 37

3.10 Simulation results for peak powers of 835 W (a), 8350 W (b) and 16700 W (c). 39

3.11 (a) Schematic drawing of UNAM OPA system. (b) The photograph of the OPA system. 40

3.12 The schematic of the experimental setup. 42

3.13 The schematic of a Czerny-Turner monochromator. Adapted from Reference [66] 43

3.14 The broadening at the end of 7 cm long nanostructured As_2Se_3 fiber at various peak powers. 46

3.15 Comparison of the spectrum at the end of 7 cm long nanostructured As_2Se_3 fiber with the pump light. 47

3.16 The spectral broadening at the end of 5 mm long nanostructured As_2Se_3 fiber for various peak powers. 48

3.17 The comparison of pump laser spectrum with 5 mm long nanostructured As_2Se_3 fiber output. 48

3.18 The broadening at the end of 5 cm long PES fiber for various input powers. 50

3.19 The broadening from 7 cm long As_2Se_3 fiber for various input powers at 2000 nm central wavelength. 51

3.20 The broadening at the end of 5 mm long As_2Se_3 fiber for various input powers at 2000 nm central wavelength. 52

3.21 The spectrum at the end of 5.5 cm long PES fiber for various input powers at 2000 nm central wavelength. 53

3.22 The broadening at the end of 5 mm long PES fiber for various input powers at 2000 nm central wavelength. 54

3.23 Comparison of the spectra of 7 cm long As_2Se_3 fiber, 5 mm long As_2Se_3 fiber; 5 cm long PES fiber and 5 mm long PES fiber. . . . 56

3.24 Comparison of the spectra of 5 mm long As_2Se_3 fiber; 5 mm long PES fiber and the monochromator response when there is no fiber. 56

3.25 (a) The two dimensional toroid analogue that is used in FDTD simulations. (b) The refractive index profile of the structure in (a). 58

3.26 (a) Simulation results for a linear toroid, i.e. $\chi^{(3)}$=0 is taken in FullWAVE with input peak power, P=10 W. (b) Simulation results for a toroid when nonlinearity of As_2Se_3 is taken into account. $\chi^{(3)}=931\times10^{-13}$ esu with input power P=2 W. (c) Simulation results for microtoroid when input power, P=10 W. Other parameters are the same as in (b). 60

4.1 The absorption and photoluminescence from DOO-PPV polymer. The data is taken using Cary 100 Bio UV-Vis spectrophotometer. Inset is the structure of DOO-PPV. 63

4.2 The refractive index and extinction coefficient for DOO-PPV polymer. 64

4.3 Main fabrication steps of the microtoroid cavity. 66

4.4 The suspended microdisks obtained when SiO_2 is grown using PECVD and Si is etched with KOH. 68

4.5 Schematics of the CO_2 laser reflow setup. 69

4.6 (a) SEM image of the obtained microdisk. (b) SEM image of the microdisk shown in (a) after being reflown with CO_2 laser. 69

4.7 (a) Surface roughness measured at the central region of the microtoroid. (b) Surface roughness measured at the rim of the microtoroid. 70

4.8 (a) SEM image of the microdisk before the reflow process. (b) Same disk after the reflow process. Note the transformed geometry in this case is not toroid; instead it is a sphere after reflow. . . . 71

4.9 (a) SEM image of the DOO-PPV coated microtoroid. (b) Optical microscope image of the of the very same microcavity in (a). (c) AFM measurement performed on the same microstructure. 72

4.10 The schematics of the experimental setup for observing laser action from DOO-PPV coated microtoroid. 73

4.11 (a) OPA excitation. (b) Emission spectrum observed from DOO-PPV coated microtoroid laser. 73

4.12 The lasing emission intensity from microtoroid vs the input pulse energy. 74

4.13 (a) The lasing spectrum obtained at 440 pJ/pulse excitation energy. (b) The FFT of the lasing spectrum shown in (a). 75

Dedicated to my family

Chapter 1

INTRODUCTION

Supercontinuum (SC) generation, substantial spectral broadening of electromagnetic radiation due to non-linear interactions with the transporting medium, has various applications in spectroscopy [1, 2], frequency metrology [3], optical coherence tomography [4, 5] and telecommunications [6, 7]. Such a broad spectrum can be obtained by effectively confining high power light pulses in highly non-linear materials maintaining very small or negative dispersion values. Supercontinuum generation was first observed by Alfano and Shapiro in 1970 [8, 9] by focusing a Nd:glass laser into borosilicate glass. Investigation of the effect in various other materials and systems; solids [10], liquids [11], gases [12] and optical waveguides [13, 14, 15] followed. The optical waveguides are particularly attractive for SC generation purposes owing to the reduced modal area, increased interaction length and design flexibility. The extent and the shape of the obtained spectrum depends on combination of several parameters: nonlinearity of the fiber, pulse duration, pump power and the relative position of zero dispersion wavelength (ZDW) of fiber to pump wavelength [16]. Photonic crystal fibers (PCF) and tapered fibers have several advantages in terms of the design flexibility they offer [14, 15].

Whispering Gallery Mode (WGM) optical microcavities confine light to micron scale areas via total internal reflection mechanism. They find application in various areas such as probing nonlinear optical effects [17, 18], telecommunications [19], lasing [20, 21], biological and chemical sensing [22] and more fundamental areas of quantum optics [23] and cavity quantum electrodynamics [24]. Among microcavities, the highest quality factors have been observed in surface-tension-induced microspheres and microtoroids [25, 26, 27].

Since its first demonstration by Armani [27] and his coworkers, the toroidal microcavities have attracted much attention and have been employed in numerous studies on nonlinear optics [17], laser action [21], optical sensing [22] and cavity quantum electrodynamics [23]. The microtoroid is obtained by laser reflow of a microdisk structure suspended on air, smoothing the surface of the cavity and enabling ultrahigh quality factors. It is this ultrahigh quality factor on the order of 10^8 in addition to integrability to chip based applications that makes the microtoroid attractive.

This thesis consists of two parts. In the first part, we have employed nanostructured chalcogenide fibers covered with polyethersulfone (PES) cladding to achieve supercontinuum generation in the near and mid infrared spectral region [28]. More specifically, the core of the fiber is As_2Se_3 with nonlinear refractive index $\sim$800 times larger than that of silica as being the major advantage. Such a superior nonlinear refractive index results in reduction in the threshold of nonlinear optical effects. Moreover, As_2Se_3 has lower dispersion in the infrared region, hence it can be useful for producing a broadband light source in the infrared region, considering its high nonlinearity. In addition to microfibers, As_2Se_3 coated toroidal microresonators were also considered to observe supercontinuum generation. When high nonlinearity of As_2Se_3 is combined with small mode volume and ultrahigh quality factor of a resonator, observation of nonlinear effects would be attained at considerably low input power levels.

The second part deals with observation of laser action from a polymer coated microtoroid [29]. The aim was to provide a chip-based, low threshold laser source by combining ultrahigh quality factor of the toroidal microcavity with a photoluminescent polymer with high quantum efficiency. Lasing was indeed observed despite employing free space excitation of the cavity, which is usually very inefficient.

The thesis is organized as follows: **Chapter** 2 gives background information on the theory behind the investigated phenomena. **Chapter** 3 describes observation of continuum generation in the microstructured chalcogenide fiber and the simulations conducted for As_2Se_3 coated microtoroid. **Chapter** 4 gives information on the fabrication of toroidal microresonators and observation of laser action when it is coated with a photoluminescent polymer, poly(dioctyloxy-*p*-phenylene-vinylene)DOO-PPV. Finally, concluding remarks and suggested future works is given in **Chapter** 5.

Chapter 2

THEORETICAL BACKGROUND

2.1 Nonlinear Optics

Nonlinear optics comes into play when the intensity of the light interacting with the medium is above a certain threshold, since the optical nonlinearities arise from the anharmonic motion of the bound electrons under an applied field which usually takes place when the applied field strength approaches ∼1 percent of the binding potential of the electron [30]. In linear optics, the induced polarization, **P** depends linearly on the applied electric field, **E**:

$$\mathbf{P} = \varepsilon_0(\chi^{(1)} \cdot \mathbf{E}) \tag{2.1}$$

However this dependence of induced polarization upon applied electric field is actually nonlinear and can be expressed as [31]:

$$\mathbf{P} = \varepsilon_0(\chi^{(1)} \cdot \mathbf{E} + \chi^{(2)} : \mathbf{EE} + \chi^{(3)} \vdots \mathbf{EEE} + \ldots) \tag{2.2}$$

In the above equations, ε_0 is the vacuum permittivity and $\chi^{(j)}$, which are tensors of rank j+1, are the j^{th} order susceptibilities of the medium.

The dominant contribution to the polarization comes from the linear susceptibility and its effects are seen through the linear refractive index n and the attenuation coefficient α. The second order susceptibility $\chi^{(2)}$ leads to nonlinear optical effects such as second harmonic generation, sum and difference frequency generations and optical parametric oscillation [32]. However, these effects can be observed in materials with noninversion symmetry only, since, otherwise $\chi^{(2)}$ becomes zero. It must also be noted that even materials with inversion symmetry can show small amounts of second order nonlinear optical effects resulting from the small asymmetries in the material. The third order susceptibility $\chi^{(3)}$ leads to third harmonic generation, four-wave mixing and the optical Kerr effect via its real part, and the imaginary part of $\chi^{(3)}$ is responsible for two photon absorption, Raman scattering and Brillouin scattering [33, 34].

In optical fibers, made from amorphous materials, the medium has inversion symmetry, so the second order nonlinear optical effects can be neglected. In this thesis, we concentrated on optical effects occurring in chalcogenide fibers. Therefore, only third order nonlinearity is considered.

2.1.1 Optical Kerr Effect

The dependence of the refractive index on the local intensity of the light is referred to as the optical Kerr effect, which results from instantaneous interaction of electromagnetic radiation with matter:

$$n(I) = n_0 + n_2 I \tag{2.3}$$

The nonlinear-index coefficient n_2 is dependent on the third order susceptibility as [31]:

$$n_2 = \frac{3}{8n_0}\mathrm{Re}(\chi^{(3)}_{xxxx}) \tag{2.4}$$

The optical Kerr effect leads to the nonlinear effects of self phase modulation (SPM) and cross phase modulation (XPM). Furthermore once phase matching

conditions are satisfied, third harmonic generation and four-wave mixing can also be observed with the same principle [31].

2.1.2 Self Phase Modulation

The intensity dependence of the refractive index as given in Eq.(2.3) results in change of the refractive index and hence change of the phase across the pulse [31]. For light of frequency ω_0 entering a medium of length L, the change in the phase can be expressed as [31]:

$$\phi_{NL}(t) = n_2 I(t) \omega_0 L/c \tag{2.5}$$

The SPM-induced spectral broadening is a consequence of the time dependence of ϕ_{NL} [31]. If instantaneous frequency $\omega(t)$ is defined as:

$$\omega(t) = \omega_0 + \delta\omega(t) \tag{2.6}$$

the difference $\delta\omega$ becomes:

$$\delta\omega(t) = -\frac{\partial \phi_{NL}}{\partial t} = -\frac{n_2 \omega_0 L}{c} \frac{\partial I(t)}{\partial t} \tag{2.7}$$

If *I(t)* is written as $I(t)=I_0|U(t)|^2$, where *U(t)* is normalized:

$$\delta\omega(t) = -\frac{n_2 \omega_0 L}{c} I_0 \frac{\partial |U(t)|^2}{\partial t} = -\frac{L}{L_{NL}} \frac{\partial |U(t)|^2}{\partial t} \tag{2.8}$$

where L_{NL} is the nonlinear length defined as:

$$L_{NL} = (\gamma P_0)^{-1} \tag{2.9}$$

with

$$\gamma = \frac{n_2 \omega_0}{c A_{eff}} \tag{2.10}$$

The time dependence of $\delta\omega$ is referred to as frequency chirp [31]. As a result of the SPM, the leading edge of the pulse is down shifted while the trailing edge is up shifted for an initially unchirped pulse, the magnitude of the frequency chirp

increases as the pulse propagates through the fiber and new frequency components are introduced. While SPM results in spectral broadening for initially unchirped or upchirped pulses, it can result in soliton formation or spectral narrowing for initially downchirped pulses [31]. SPM is one of the main mechanisms for supercontinuum generation when a fiber is pumped with ultrashort pulses in both normal and anomalous group velocity dispersion regimes.

2.1.3 Cross Phase Modulation

When two optical fields propagate inside a fiber, they can interact with each other. The phenomenon where the intensity of one beam causes a phase shift in the other beam, is called cross phase modulation (XPM). XPM can occur either between the two orthogonally polarized components of the optical field or between two optical fields of different wavelengths. XPM is an elastic effect; no energy is transferred between the propagating fields. The change in the refractive index due to combined effect of SPM and XPM can be found as follows [31]:

$$\mathbf{E}(\mathbf{r},t) = \frac{1}{2}\widehat{x}[E_1 exp(-i\omega_1 t) + E_2 exp(-i\omega_2 t)] + c.c. \tag{2.11}$$

substituting Eq.(2.11) into Eq.(2.2), and looking for nonlinear polarization terms with *exp(-iω$_j$t)* for j=1, 2,

$$P_{NL}(\omega_j) = (\frac{3\varepsilon_0}{4})\chi^{(3)}_{xxxx}(|E_j|^2 + 2|E_{3-j}|^2)E_j = \varepsilon_0 \varepsilon_j^{NL} E_j \tag{2.12}$$

using $\varepsilon_j = \varepsilon_j^L + \varepsilon_j^{NL} = (n_j^L + \Delta n_j)^2$ with the assumption $\Delta n_j << n_j^L$:

$$\Delta n_j \approx \varepsilon_j^{NL}/2n_j \approx n_2(|E_j|^2 + 2|E_{3-j}|^2) \tag{2.13}$$

where

$$n_2 = \frac{3\chi^{(3)}_{xxxx}}{8n_j^L} \tag{2.14}$$

is obtained. The accumulated nonlinear phase shift is given by:

$$\phi_j^{NL}(z) = (\omega_j/c)\Delta n_j z = n_2(\omega_j/c)(|E_j|^2 + 2|E_{3-j}|^2)z \tag{2.15}$$

The first term in this equation is the contribution of SPM and the second term is the contribution of the XPM to nonlinear phase shift. Note that the effect of XPM is twice as much as the effect of SPM for the same intensity. When SPM acts alone, the induced spectral broadening is symmetric in shape. However, the combined effect of SPM and XPM results in an asymmetrically broadened spectrum if there is a group velocity mismatch between the two pulses.

2.1.4 Four Wave Mixing

Four Wave Mixing (FWM) is a third order parametric process. In parametric processes, the initial and the final quantum mechanical states of the system are identical [32]. The medium plays a passive role in parametric processes, so energy is not transferred between the optical wave and medium. Parametric processes depend on both second and third order susceptibility of the material. Therefore, depending on the magnitude of those quantities, second harmonic generation and sum or difference frequency mixing can be observed in the material as second order parametric processes in addition to FWM, third harmonic generation and parametric amplification as third order parametric processes. FWM is a nonlinear interaction between four optical waves where photons at certain frequencies are annihilated in order to create photons at new frequencies.

There are two types of FWM [31]: in the first type, three photons transfer their energy to a photon at a different wavelength: $\omega_4 = \omega_1 + \omega_2 + \omega_3$. When the frequencies $\omega_1 = \omega_2 = \omega_3$, the process is called third harmonic generation, when $\omega_1 = \omega_2 \neq \omega_3$ it is called frequency conversion. In the second type, photons at frequencies of ω_1 and ω_2 are annihilated to create photons at frequencies of ω_3 and ω_4: $\omega_1 + \omega_2 = \omega_3 + \omega_4$.

FWM is hard to observe since it requires certain phase matching conditions to be satisfied which means that the wave vectors of interacting optical fields

must be matched in addition to matching of frequencies:

$$k_1 + k_2 + k_3 = k_4 \tag{2.16a}$$

$$k_1 + k_2 = k_3 + k_4 \tag{2.16b}$$

for the first and second types respectively.

However, it is easier to obtain phase matching if $\omega_1 = \omega_2$ in the second type of FWM. In this case, two photons of frequency ω_1 are annihilated to create ω_3 and ω_4 photons located symmetrically around ω_1. ω_3 is taken to be the low frequency sideband, called the Stokes band and ω_4 is taken to be the high frequency sideband and is called the anti-Stokes band [31]. FWM is an important process leading to supercontinuum generation for pulses with durations on the order of picoseconds in the anomalous group velocity dispersion (GVD) regime. It can also be observed in the normal GVD regime with less efficiency.

2.1.5 Stimulated Raman Scattering

Stimulated Raman Scattering (SRS) is an inelastic scattering process, in contrast to previously discussed nonlinear optical effects. In this case, energy is transferred between the photons of incoming light and optical phonons of the medium. SRS is an example of non-parametric processes as a result of the imaginary part of $\chi^{(3)}$.

In spontaneous Raman scattering, incoming light is scattered by the medium with a new frequency due to transfer of energy between photons and optical phonons. If the scattered photons have a lower frequency than the incoming photons, the scattering is referred to as Stokes scattering, if the scattered photons have a higher frequency than they originally had, the scattering is called as anti-Stokes scattering. However, the spontaneous Raman scattering is a weak process. The scattering cross section is $\sim 10^{-6}$ cm^{-1}. Therefore, when propagating through 1 cm of scattering medium, $\sim 10^{-6}$ of the incident light will be

converted to Stokes frequency [32]. However, in case of an intense laser beam propagating in the medium, stimulated Raman scattering takes place as a much more efficient mechanism where ∼10% of the incident light may be converted to Stokes frequency. SRS can be investigated using the following equations for the CW or quasi-CW case [31]:

$$\frac{dI_s}{dz} = g_R I_p I_s - \alpha_s I_s \tag{2.17}$$

$$\frac{dI_p}{dz} = -\frac{\omega_p}{\omega_s} g_R I_p I_s - \alpha_p I_p \tag{2.18}$$

where I_p and I_s are the intensities; ω_p and ω_s are the frequencies of the pump and Stokes waves and α_p and α_s are the losses at the pump and Stokes waves respectively.

2.1.6 Stimulated Brillouin Scattering

Stimulated Brillouin Scattering (SBS) occurs when the intensity of the light in a medium is high enough to generate acoustic vibration. The generated acoustic waves affect the density of the material and change its refractive index. SBS stems from the scattering of light due to this index modulation [33]. SBS can occur at much lower optical power levels than those needed for SRS. The main difference between SBS and SRS is that acoustic phonons play role in SBS while optical phonons play role in SRS. Similar to SRS, a Stokes wave is generated in SBS, too. However, the difference between the pump and Stokes frequencies is much lower than in the case of SRS. Moreover, SBS generated Stokes wave travels in the backward direction in an optical fiber while the SRS generated Stokes wave can travel in both directions.

2.1.7 Pulse Propagation in Nonlinear Media

While a pulse is propagating in a medium both nonlinearity and dispersion acts on the pulse at the same time. Hence, the two effects should be considered together for a correct analysis. Therefore, we start this section by describing chromatic dispersion.

Chromatic Dispersion

The dependence of the group velocity of a pulse to frequency is defined as the chromatic dispersion which consists of waveguide and material dispersions. Material dispersion is the frequency dependence of the refractive index of bulk material and waveguide dispersion is the change in mode confinement profile with optical frequency [33]. Far from medium resonances, the refractive index of a material can be approximated by the Sellmeier equation [31]:

$$n^2(\omega) = 1 + \sum_{j=1}^{m} \frac{B_j \omega_j^2}{\omega_j^2 - \omega^2} \tag{2.19}$$

where ω_j is the resonance frequency and B_j is the strength of the j^{th} resonance.

The mode propagation constant, β can be expanded in a Taylor series around the central frequency ω_0 [31]:

$$\beta(\omega) = n(\omega)\frac{\omega}{c} = \beta_0 + \beta_1(\omega - \omega_0) + \frac{1}{2}\beta_2(\omega - \omega_0)^2 + ... \tag{2.20}$$

here,

$$\beta_m = \left(\frac{d^m \beta}{d\omega^m}\right)_{\omega=\omega_0} \tag{2.21}$$

β_1 is related to the group velocity as:

$$\beta_1 = \frac{1}{V_g} = \frac{n_g}{c} = \frac{1}{c}\left(n + \omega\frac{dn}{d\omega}\right) \tag{2.22}$$

β_2 is the group velocity dispersion parameter, representing the frequency dependence of the group velocity:

$$\beta_2 = \frac{1}{c}\left(2\frac{dn}{d\omega} + \omega\frac{d^2n}{d\omega^2}\right) \tag{2.23}$$

When $\beta_2 > 0$, the fiber is said to exhibit normal dispersion and when $\beta_2 < 0$, the fiber exhibits anomalous dispersion. In the normal dispersion regime, high frequency components of an optical pulse travel slower than the low frequency components and the opposite occurs in the anomalous dispersion regime. Another parameter, D, called the dispersion parameter, can also be used instead of β_2 [31]:

$$D = \frac{d\beta_1}{d\lambda} = -\frac{2\pi c}{\lambda^2}\beta_2 \approx -\frac{\lambda}{c}\frac{d^2 n}{d\lambda^2} \tag{2.24}$$

The total chromatic dispersion of a waveguide can be calculated as follows: The effective refractive indices of the waveguide can be determined for different wavelengths through a numerical method, and the found n_{eff} values can be fit to the Sellmeier equation for obtaining dispersion through:

$$D = -\frac{\lambda}{c}\frac{d^2 n_{eff}}{d\lambda^2} \tag{2.25}$$

Since it is usually very difficult to tune material dispersion, tailoring the waveguide dispersion can be useful for several applications including dispersion shifted fibers where the zero dispersion wavelength (ZDW) is shifted to the desired wavelength, e.g. to a wavelength where the material absorption is smaller. Such fibers are especially important in telecommunications as well as in supercontinuum generation. In the latter case, dispersion has a detrimental effect on the spectral broadening of pulse propagating in the fiber. Therefore, if the dispersion is modified so that the pulse wavelength is close to the fiber's ZDW, the observed broadening effect will be much stronger.

Nonlinear Schrödinger Equation

Let us begin the discussion of pulse propagation in dispersive and nonlinear media by writing the Maxwell equations:

$$\nabla \times \mathbf{E} = -\frac{\partial \mathbf{B}}{\partial t} \tag{2.26}$$

$$\nabla \times \mathbf{H} = \mathbf{J} + \frac{\partial \mathbf{D}}{\partial t} \tag{2.27}$$

$$\nabla \cdot \mathbf{D} = \rho_f \tag{2.28}$$

$$\nabla \cdot \mathbf{B} = 0 \tag{2.29}$$

where $\mathbf{E}$ and $\mathbf{H}$ are the electric and magnetic field vectors, and $\mathbf{D}$ and $\mathbf{B}$ are the corresponding electric and magnetic flux densities. $\mathbf{J}$ is the current density vector and ρ_f is the charge density. In an optical fiber, $\mathbf{J}$ and ρ_f are 0.

$\mathbf{D}$ and $\mathbf{B}$ relate to $\mathbf{E}$ and $\mathbf{H}$ through,

$$\mathbf{D} = \varepsilon_0 \mathbf{E} + \mathbf{P} \tag{2.30}$$

$$\mathbf{B} = \mu_0 \mathbf{H} + \mathbf{M} \tag{2.31}$$

Here, ε_0 is the vacuum permittivity, μ_0 is the vacuum permeability, $\mathbf{P}$ is the induced electric polarization vector and $\mathbf{M}$ is the induced magnetic polarization vector. Since optical fibers are nonmagnetic, $\mathbf{M}$ is 0.

To find the wave equation describing the propagation of light in the fiber, take curl of Eq.(2.26) to obtain:

$$\nabla \times \nabla \times \mathbf{E} = -\frac{1}{c^2}\frac{\partial^2 \mathbf{E}}{\partial t^2} - \mu_0 \frac{\partial^2 \mathbf{P}}{\partial t^2} \tag{2.32}$$

use the relation

$$\nabla \times \nabla \times \mathbf{E} = \nabla(\nabla \cdot \mathbf{E}) - \nabla^2 \mathbf{E} = -\nabla^2 \mathbf{E} \tag{2.33}$$

since $\nabla \cdot \mathbf{E} = 0$. Then, Eq.(2.32) becomes:

$$\nabla^2 \mathbf{E} - \frac{1}{c^2}\frac{\partial^2 \mathbf{E}}{\partial t^2} - \mu_0 \frac{\partial^2 \mathbf{P}}{\partial t^2} = 0 \tag{2.34}$$

When far from medium resonances, Eq.(2.2) can be used to define $\mathbf{P}$, which can be divided into linear and nonlinear components:

$$\mathbf{P}(\mathbf{r}, \mathbf{t}) = \mathbf{P}_L(\mathbf{r}, t) + \mathbf{P}_{NL}(\mathbf{r}, t) \tag{2.35}$$

which are related to the electric field through the following equations:

$$\mathbf{P}_L(\mathbf{r},t) = \varepsilon_0 \int_{-\infty}^{\infty} \chi^{(1)}(t-t') \cdot \mathbf{E}(\mathbf{r},t')dt' \tag{2.36}$$

$$\mathbf{P}_{NL}(\mathbf{r},t) = \varepsilon_0 \int\int\int_{-\infty}^{\infty} \chi^{(3)}(t-t_1,t-t_2,t-t_3)\vdots\mathbf{E}(\mathbf{r},t_1)\mathbf{E}(\mathbf{r},t_2)\mathbf{E}(\mathbf{r},t_3)dt_1dt_2dt_3 \tag{2.37}$$

when the second order susceptibility, $\chi^{(2)}$ is taken as zero. When nonlinear response of the medium is considered to be instantaneous, $\mathbf{P}_{NL}(\mathbf{r},t)$ can be written as:

$$\mathbf{P}_{NL}(\mathbf{r},t) = \varepsilon_0\chi^{(3)}\vdots\mathbf{E}(\mathbf{r},t)\mathbf{E}(\mathbf{r},t)\mathbf{E}(\mathbf{r},t) \tag{2.38}$$

Taking the assumptions made above into consideration and using $\mathbf{P}_L(\mathbf{r},t) = \varepsilon_0\chi^{(1)}\mathbf{E}(\mathbf{r},t)$, the wave equation, Eq.(2.34) can be written in the Fourier domain as:

$$\nabla^2\mathbf{E}(\omega) + \frac{\omega^2}{c^2}\mathbf{E}(\omega) + \frac{\omega^2}{c^2}\chi^{(1)}\mathbf{E}(\omega) = -\mu_0\omega^2\mathbf{P}_{NL} \tag{2.39}$$

Now, introduce the slowly varying envelope approximation and write the electric field as multiplication of a fast varying field and a slowly varying field:

$$\mathbf{E}(\mathbf{r},t) = \frac{1}{2}\hat{x}[E(\mathbf{r},t)exp(-i\omega_0 t) + c.c.] \tag{2.40}$$

We can apply this to $\mathbf{P_L}$ and $\mathbf{P_{NL}}$ as well:

$$\mathbf{P_L}(\mathbf{r},t) = \frac{1}{2}\hat{x}[P_L(\mathbf{r},t)exp(-i\omega_0 t) + c.c.] \tag{2.41}$$

$$\mathbf{P_{NL}}(\mathbf{r},t) = \frac{1}{2}\hat{x}[P_{NL}(\mathbf{r},t)exp(-i\omega_0 t) + c.c.] \tag{2.42}$$

$P_{NL}(\mathbf{r},t)$ can be written as [31]:

$$P_{NL}(\mathbf{r},t) \approx \varepsilon_0\varepsilon_{NL}E(\mathbf{r},t) \tag{2.43}$$

and, substituting Eq.(2.40) in Eq.(2.38), using Eq.(2.42) and neglecting the $3\omega_0$ terms,

$$\varepsilon_{NL} = \frac{3}{4}\chi^{(3)}_{xxxx}|E(\mathbf{r},t)|^2 \tag{2.44}$$

is found. Then, substituting Eq.(2.43) in Eq.(2.39) and using $\varepsilon(\omega) = 1+\chi^{(1)}_{xx}(\omega)+\varepsilon_{NL}$, Eq.(2.39) can be written as:

$$\nabla^2 E + \varepsilon(\omega)\frac{\omega^2}{c^2}E = 0 \tag{2.45}$$

which can be solved by introducing:

$$E(\mathbf{r},\omega) = F(x,y)\widetilde{A}(z,\omega)exp(i\beta_0 z) \tag{2.46}$$

where β_0 is the wave number, $F(x,y)$ represents the modal distribution and $\widetilde{A}(z,\omega)$ represents the slowly varying pulse envelope. The equations for $\widetilde{A}(z,\omega)$ and $F(x,y)$ can be written as [31]:

$$\frac{\partial^2\widetilde{A}}{\partial z^2} + 2i\beta_0\frac{\partial\widetilde{A}}{\partial z} + (\widetilde{\beta}^2 - \beta_0^2)\widetilde{A} = 0 \tag{2.47}$$

$$\frac{\partial^2 F}{\partial x^2} + \frac{\partial^2 F}{\partial y^2} + [\varepsilon(\omega)k_0^2 - \widetilde{\beta}^2]F = 0 \tag{2.48}$$

$\partial^2\widetilde{A}/\partial z^2$ term in Eq.(2.47) can be neglected since $\widetilde{A}(z,\omega)$ is a slowly varying function of z. $\varepsilon(\omega)$ is approximated by [31]:

$$\varepsilon = (n+\Delta n)^2 \approx n^2 + 2n\Delta n \tag{2.49}$$

with

$$\Delta n = n_2|E|^2 + \frac{i\widetilde{\alpha}}{2k_0} \tag{2.50}$$

and

$$\widetilde{\alpha} = \alpha + \alpha_2|E|^2 \tag{2.51}$$

$\widetilde{\beta}$ can be found by solving Eq.(2.48) using first-order perturbation theory. First, $\beta(\omega)$ is found using $\varepsilon = n^2$ and then, effect of Δn is included to find [31]:

$$\widetilde{\beta}(\omega) = \beta(\omega) + \Delta\beta \tag{2.52}$$

and

$$\Delta\beta = \frac{k_0\int\int_{-\infty}^{\infty}\Delta n|F(x,y)|^2 dxdy}{\int\int_{-\infty}^{\infty}|F(x,y)|^2 dxdy} \tag{2.53}$$

Using Eq.(2.52) and approximating $\widetilde{\beta}^2 - \beta_0^2$ by $2\beta_0(\widetilde{\beta} - \beta_0)$, Eq.(2.47) can be written as [31]:

$$\frac{\partial \widetilde{A}}{\partial z} = i[\beta(\omega) + \Delta\beta - \beta_0]\widetilde{A} \tag{2.54}$$

which implies that as the pulse propagates in the fiber, each spectral component accumulates a frequency and intensity dependent phase shift [31]. Now, use the Taylor expansion of $\beta(\omega)$ about ω_0:

$$\beta(\omega) = \beta_0 + \beta_1(\omega - \omega_0) + \frac{1}{2}\beta_2(\omega - \omega_0)^2 + \frac{1}{6}\beta_3(\omega - \omega_0)^3 + \dots \tag{2.55}$$

where

$$\beta_m = \left(\frac{d^m\beta}{d\omega^m}\right)_{\omega=\omega_0} for\ m = 1, 2, \dots \tag{2.56}$$

By neglecting the high order terms, the equation for $A(z,t)$, in time domain, can be written as:

$$\frac{\partial A}{\partial z} + \beta_1\frac{\partial A}{\partial t} + \frac{i\beta_2}{2}\frac{\partial^2 A}{\partial t^2} + \frac{\alpha}{2}A = i\gamma|A|^2A \tag{2.57}$$

and is known as the Nonlinear Schrödinger Equation (NLSE). Here, β_1 is the group delay; β_2 is the group velocity dispersion, α represents the losses and γ is the nonlinear parameter defined as:

$$\gamma = \frac{n_2\omega_0}{cA_{eff}} \tag{2.58}$$

where A_{eff} is the effective core area, defined as [31]:

$$A_{eff} = \frac{(\int\int_{-\infty}^{\infty}|F(x,y)^2|dxdy)^2}{\int\int_{-\infty}^{\infty}|F(x,y)|^4dxdy} \tag{2.59}$$

The NLSE describes the propagation of a pulse inside a single mode optical fiber. The effects of fiber losses, chromatic dispersion and nonlinearity are included in the equation through α, β_2 and γ respectively.

The spectral broadening of a pulse inside a fiber can be understood by taking into account the combined effects of dispersion and nonlinearity. Basically, solving the NLSE should give an idea on the evolution of the pulse despite the

fact that inelastic scattering is not considered. Usually, the NLSE is solved numerically, since analytic solution is not always available, to investigate the pulse propagation. Most commonly used method for this purpose is the Split-Step Fourier Method which will be described in Chapter 3.

Mechanisms leading to supercontinuum generation, including SPM, XPM, Raman scattering, FWM and soliton dynamics, will be qualitatively described in Chapter 3. Such mechanisms can be efficiently observed depending on the duration of pulse and the position of central wavelength with respect to the ZDW. As for the pump pulses and the fiber used in this thesis, the spectral broadening is mainly a result of SPM effect.

2.2 Laser Action

In this section, some basic concepts of laser action mechanism will be given.

2.2.1 Absorption, Spontaneous Emission and Stimulated Emission

In our context, three interactions of light with matter is important and will be explained: absorption, spontaneous emission and stimulated emission.

In **absorption**, incoming electromagnetic wave, having energy $h\nu$ can be absorbed by the atom and excite its electron from ground state to an excited state if the energy difference between the two states is $h\nu$.

The same atom would then reduce its energy by relaxing from excited state to ground state. If this transition is a radiative transition, then the atom emits a photon of energy $h\nu$. If the transition is non-radiative then the atom will not emit any photons and energy will be transferred to non-radiative relaxation mechanisms such as molecular vibrations. In reality, energy is distributed between

radiative and non-radiative channels in a molecule, therefore the emitted photon usually has lower energy than $h\nu$. This process is called **spontaneous emission**. Finally, if a photon having energy $h\nu$ interacts with the atom when it is in its excited state, the atom goes back to its ground state by emitting another photon having the same energy and phase with the incoming photon; this process is called **stimulated emission**.

Now, let us look at the relations between absorption, stimulated emission and spontaneous emission in a two-level system:
Let's assume that the ground level population is N_1 and the upper level population is N_2. There are three processes leading to a change in the number of electrons between these two levels, as defined above. The rate for spontaneous emission, r_1 is:

$$r_1 = AN_2 \tag{2.60}$$

where A is the spontaneous emission probability. The rate for stimulated emission r_2 is:

$$r_2 = B_{21}N_2\rho \tag{2.61}$$

where B_{21} is the stimulated emission probability and ρ is the photon density. The rate for absorption is:

$$r_3 = B_{12}N_1\rho \tag{2.62}$$

where B_{12} is the absorption probability. In thermodynamic equilibrium, the number of transitions from the ground level to the upper level is equal to the number of transitions from the upper level to the ground level:

$$r_1 + r_2 = r_3 \tag{2.63}$$

$$B_{12}N_1\rho = AN_2 + B_{21}N_2\rho \tag{2.64}$$

ρ can be found as:

$$\rho = \frac{AN_2}{B_{12}N_1 - B_{21}N_2} \tag{2.65}$$

From Planck's radiation law, ρ is:

$$\rho = \frac{8\pi h\nu^3}{c^3}\frac{1}{exp((E_2 - E_1)/kT) - 1} \tag{2.66}$$

From Boltzmann distribution,

$$\frac{N_2}{N_1} = \exp\frac{-(E_2 - E_1)}{kT} \tag{2.67}$$

Noting B_{21}=B_{12}=B,

$$\frac{8\pi h\nu^3}{c^3}\frac{1}{\frac{N_1}{N_2} - 1} = \frac{A}{B}\frac{1}{\frac{N_1}{N_2} - 1} \tag{2.68}$$

Finally,

$$\frac{A}{B} = \frac{8\pi h\nu^3}{c^3} \tag{2.69}$$

can be obtained. For lasing to occur, stimulated emission rate should exceed the absorption and spontaneous emission rates.

$$\frac{r_2}{r_1} = \frac{1}{\frac{N_1}{N_2} - 1} \tag{2.70}$$

$$\frac{r_2}{r_3} = \frac{N_2}{N_1} \tag{2.71}$$

From above equations, it can be seen that, for stimulated emission rate to exceed spontaneous emission rate and absorption rate, the population of the upper level must be greater than that of the lower level, however, this can never be attained in a two-level system since once the number of electrons in the ground and excited state is the same the stimulated emission rate and absorption rate become equal, making the material optically transparent to incoming electromagnetic radiation. This situation is called "two level saturation" [35]. However, this condition can be met in three (or higher) level systems.

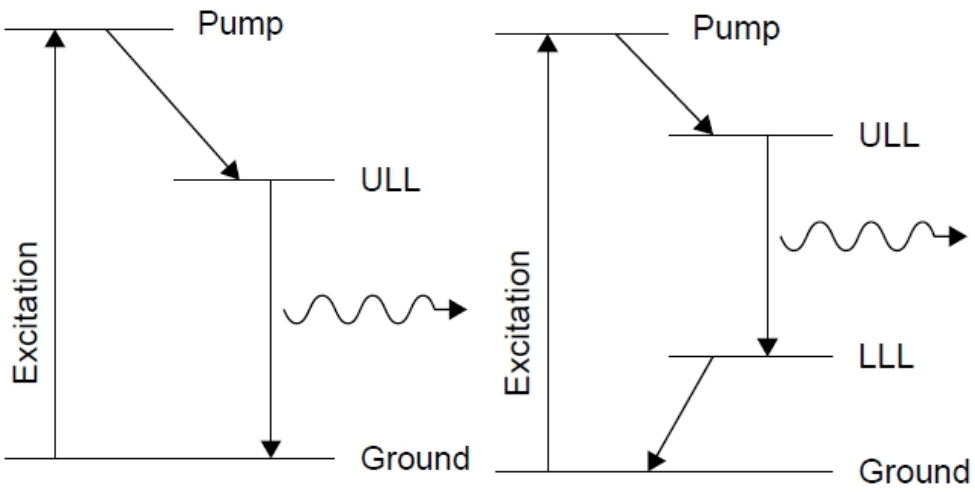

Figure 2.1: (a) Three-level laser system. (b) Four-level laser system. Adapted from Reference [36].

Figure 2.1 represents the three and four level system schematics. When a three-level system is pumped by incoming EM wave, atoms are excited to the pump level, from which they rapidly decay non-radiatively to the upper lasing level which has a long lifetime enabling population inversion and consequently lasing action to occur. When a four-level system is pumped by incoming EM wave, atoms are excited to the pump level and quickly decay non-radiatively to the upper lasing level. Generally, upper lasing level has longer lifetime than the lower one and since the lower lasing level is assumed to be initially empty, population inversion is easily achieved [36].

2.2.2 Superradiance, Superfluorescence, Amplified Spontaneous Emission

Superradiance is the collective emission from an ensemble of excited atoms or ions where the coherence of excitation light results in a macroscopic dipole moment [37]. The peak power of the emitted light is proportional to square

of the number of atoms. The time evolution of the emission has a bell shaped curve with time duration much smaller than the spontaneous emission lifetime. Population inversion is obtained after a certain threshold. The length of active material is smaller than a characteristic cooperative length, depending on the initial population inversion. Light will be emitted in a solid angle of diffraction angle, λ/D where D is the diameter of the active material [35].

Superfluorescence is the collective emission from an ensemble of excited atoms or ions, like superradiance [37]. There are many similarities between two processes. The main difference is that, the atoms (or ions) are initially incoherently excited and there is no macroscopic dipole moment created by the excitation process. Moreover, the pulse maximum appears after some delay [37].

Amplified Spontaneous Emission (**ASE**) is also known as superluminescence and is spontaneously emitted radiation enhanced by [37]. Here, the fluorescence of the molecules around the center of a solid angle will be amplified more compared to the rest, resulting in a highly directional emission. The time evolution is again a bell shaped curve with a time duration much smaller than spontaneous emission lifetime. Here, the emitters are not interacting with each other and there is neither a strict threshold nor a critical cooperative length. The emission angle is determined by geometrical factors and is usually larger than that of superradiance[35].

For a laser to operate, there has to be an active medium, in which population inversion is achieved by pumping the system and there has to be a cavity providing the positive feedback necessary for amplification. In this thesis, DOO-PPV is used as the active medium and pumping is provided optically by an OPA-800C laser system where the employed cavity is a toroidal microresonator.

2.3 Whispering Gallery Mode Resonators

Whispering Gallery Mode (WGM) microcavities confine EM radiation via total internal reflection (TIR) mechanism in a micron scale area [38], where light follows the periphery of the microstructure. Examples of WGM microcavities can be seen in Figure 2.2. Such microcavities can be characterized in terms of their quality factor (Q), free spectral range (FSR), finesse, mode volume and modal distribution.

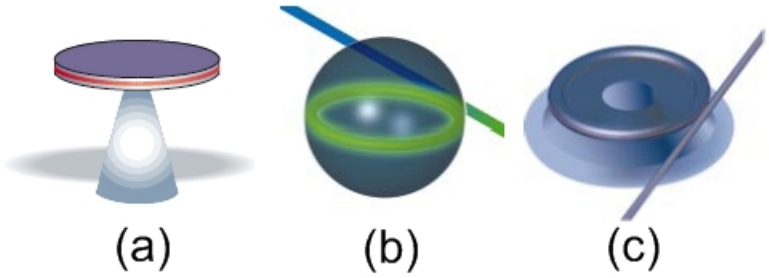

Figure 2.2: Examples of different WGM microresonators: (a) microdisk, (b) microsphere, (c) microtoroid. Adapted from Reference [38].

2.3.1 Optical Modes

Optical modes of a WGM microresonator can be found by solving the Helmholtz equation in the corresponding geometry. In the most widely studied sphere geometry, mode solving procedure starts by writing the Helmholtz equation in spherical coordinates:

$$\frac{1}{r^2}\frac{\partial}{\partial r}(r^2\frac{\partial \psi}{\partial r}) + \frac{1}{r^2\sin\theta}\frac{\partial}{\partial \theta}(\sin\theta\frac{\partial \psi}{\partial \theta}) + \frac{1}{r^2\sin^2\theta}\frac{\partial^2\psi}{\partial \phi^2} + k^2\psi = 0 \qquad (2.72)$$

where k is the wave vector inside the medium, $k{=}\omega\sqrt{\mu\epsilon}$.

If the direction of polarization can be assumed to be constant along a fixed set of spherical coordinates throughout all space, the solutions to Eq.(2.72) in

spherical coordinates are separable[39]:

$$\psi(r,\theta,\phi) = \psi_r(r)\psi_\theta(\theta)\psi_\phi(\phi) \tag{2.73}$$

the radial component:

$$\frac{d}{dr}(r^2\frac{d\psi_r}{dr}) + (k^2r^2 - l(l+1))\psi_r = 0 \tag{2.74}$$

the polar component:

$$\frac{1}{\sin\theta}\frac{d}{d\theta}(\sin\theta\frac{d\psi_\theta}{d\theta}) + (l(l+1) - \frac{m^2}{\sin^2\theta})\psi_\theta = 0 \tag{2.75}$$

the azimuthal component:

$$\frac{d^2\psi_\phi}{d\phi} + m^2\psi_\phi = 0 \tag{2.76}$$

the solution for the azimuthal component is:

$$\psi_\phi = \frac{1}{\sqrt{2\pi}}\exp(\mp im\phi) \tag{2.77}$$

the solution for the polar component is defined by the Legendre polynomials, $\mathrm{P}_m^l(\cos\theta)$ and the solution for the radial component can be written in terms of Bessel functions.

Despite the fact that the optical modes of a dielectric sphere is widely studied and has an analytical solution, modes of a toroidal microcavity cannot be analytically solved since only one coordinate of the wave equation separates, reducing it to a two-dimensional Helmholtz equation [40]. Nevertheless, such modes can be found using numerical methods and have been investigated in several studies [41, 42].

2.3.2 Free Spectral Range

The free spectral range (FSR), is defined as the wavelength spacing between successive longitudinal modes of a Fabry-Perot resonator [42]. By considering the WGM microresonator as a Fabry-Perot resonator wrapped on to itself; for

azimuthally symmetric resonator of radius R and effective refractive index n_{eff}, the FSR can be approximated as [42]:

$$\Delta\lambda_{FSR} = \frac{\lambda^2}{2\pi n_{eff} R} \tag{2.78}$$

2.3.3 Finesse

Finesse (F) is defined as the ratio of cavity mode spacing to cavity bandwidth [42]:

$$F = \frac{\Delta\lambda_{FSR}}{\Delta\lambda} = \frac{\lambda Q}{2\pi n_{eff} R} \tag{2.79}$$

This quantity gives information on the spectral noise/power amount of a resonant filter and the amount of energy amplification in a laser system [42].

2.3.4 Mode Volume

The mode volume of a microcavity describes confinement of light inside the resonator and can be especially important in several applications such as nonlinear optics where the optical intensity plays a crucial role. The modal volume can be defined as [42]:

$$V_m = \frac{(\int_V |\overrightarrow{E}|^2 d^3\overrightarrow{r})^2}{\int_V |\overrightarrow{E}|^4 d^3\overrightarrow{r}} \tag{2.80}$$

2.3.5 Quality Factor

Quality factor of a microcavity describes how long the light stays inside the cavity or equivalently how sharp the cavity modes are. The definition of the quality factor is [42]:

$$Q = \frac{\lambda}{\Delta\lambda} = \omega\tau \tag{2.81}$$

This quantity is closely related to the cavity losses; the better is the confinement inside the cavity, the higher is the quality factor.

The total quality factor of a cavity can be written as a sum of several independent contributions to the loss [42]:

$$Q_{total}^{-1} = Q_{material}^{-1} + Q_{WGM}^{-1} + Q_{ss}^{-1} + Q_{contamination}^{-1} + Q_{coupling}^{-1} \tag{2.82}$$

Here, $Q^{-1}{}_{material}$ term is related to material losses and $Q^{-1}{}_{WGM}$ indicates the radiation losses, arising from TIR at the curved interface, which increases as the curvature of microcavity increases. $Q^{-1}{}_{ss}$ corresponds to the losses due to scattering centers at the resonator surface. $Q^{-1}{}_{contamination}$ indicates the losses from surface contaminants and $Q^{-1}{}_{coupling}$ is the loss due to coupling of light to and from the cavity. The intrinsic quality factor of the microcavity is defined as [42]:

$$Q_{intrinsic} = Q_{material}^{-1} + Q_{WGM}^{-1} + Q_{ss}^{-1} + Q_{contamination}^{-1} \tag{2.83}$$

2.3.6 Cavity Build-up Factor

The cavity build-up factor indicates how much power circulates inside a cavity compared to the pump power [42]:

$$\frac{P_{circ}}{P_{input}} = \frac{\lambda Q_0}{\pi^2 n R} \frac{K}{(1+K)^2} \tag{2.84}$$

where Q_0 is the intrinsic quality factor of the cavity and $K \equiv Q_{intrinsic}/Q_{coupling}$

Chapter 3

CONTINUUM GENERATION in MICROSTRUCTURED CHALCOGENIDE OPTICAL FIBER and TOROIDAL MICRORESONATOR

3.1 Introduction

Supercontinuum generation is a process where the spectrum of the input laser pulse is largely broadened and takes place when ultrashort pulses are propagated through a nonlinear medium. The physical mechanisms behind supercontinuum generation are numerous and include self phase modulation, Raman processes, four-wave mixing and solitonic interactions, depending on the pump laser type

and the medium properties. Supercontinuum (SC) generation has various applications in spectroscopy [1, 2] optical frequency metrology [3], optical coherence tomography [4, 5], device characterization [43] and telecommunications [6, 7].

SC generation provides a broadband coherent light source [44] which combines wide spectrum, high brightness and collimation that makes it preferable over other broadband light sources. Figure 3.1 compares the brightness and spectrum obtained from different broadband sources. The SC spectrum given in this figure was obtained by using a NL-1040 PCF [45], pumped by a nanosecond 1064 nm microchip laser and can be realized to offer a better output than the compared broadband sources in terms of brightness and broadness of the spectrum.

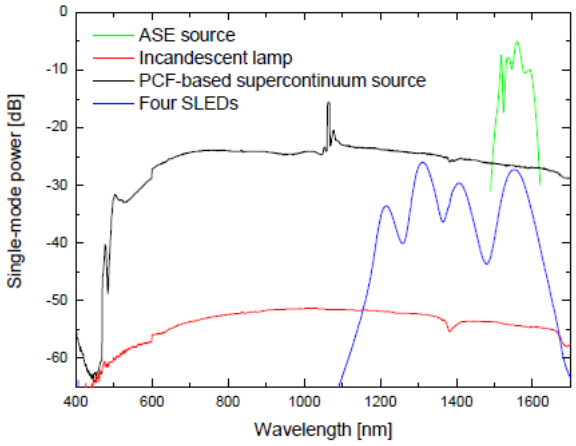

Figure 3.1: Comparison of different broadband sources. Adapted from Reference [45].

Supercontinuum generation was first observed by Alfano and Shapiro in 1970 [8, 9] by focusing a Nd:glass laser into borosilicate glass. In the experiment, second harmonic generated pulses of 530 nm wavelength, 4-8 ps pulse width and 5 mJ pulse energy were used, producing a 300 nm wide spectrum. Since this first experiment, numerous studies have been conducted on SC generation, in solids [10], liquids [11], gases [12] and in optical waveguides [13, 14, 15]. Due to reduced modal area, increased interaction length and design flexibility, optical

waveguides are of special interest for observation of non-linear effects, especially SC generation. Among various types of waveguides, the most extensively studied geometry is the fiber geometry where SC generation was first observed by Stolen and Lin in 1976 [46]. In this experiment, a 10 ns dye laser with 20 kW peak power was used as the pump and coupled to a 19.5 m long silica core fiber with core diameter of 7 μm. The observed broadening at the end of the fiber was between 110-180 nm when intensity inside the fiber was 10^9 W/cm^2.

The obtained spectrum at the end of the fiber shows different properties depending on the position of pump wavelength relative to zero dispersion wavelength (ZDW) and duration of the pump pulse. For example, when input pulse has a time duration in the femtosecond range and the central wavelength is in the anomalous dispersion regime, the SC generation is dominated by soliton dynamics where initially formed high order soliton experiences some broadening due to SPM breaks up into a series of fundamental solitons, which is also called soliton fission. The soliton fission can be triggered by Raman scattering or higher order dispersion. For pulse durations longer than 200 fs, Raman scattering is more dominant yet for pulse durations less than 20 fs, the high order dispersion dominates in triggering the soliton fission [47, 16]. When ultrashort pulse has a central wavelength in the normal GVD regime of the fiber, SPM is the dominant nonlinear process leading to SC generation. When input pulse has a longer time duration, in the picosecond regime, the soliton dynamics still play a role if the pulse is in the anomalous GVD regime of the fiber. However, the fission length for the initial high order soliton is much longer than that of fs regime and in the beginning of propagation distance, four-wave mixing and Raman scattering processes dominate. The maximum Raman gain is significantly smaller than the gain for phase-matched four-wave mixing and becomes dominant only when large phase mismatches or large walk off effects are present in the system. In normal GVD regime, the four-wave mixing processes are harder to observe and Raman scattering, in addition to SPM is the dominant spectral broadening process [16].

The central wavelength of the pump laser is not always tunable, however, it is possible to design the fiber accordingly to have the desired ZDW. For example, the photonic crystal fiber (PCF) is one type of fiber that offers great design flexibility. PCF was first proposed and manufactured by Kaiser and colleagues in 1973 [48]. However the technology did not allow manufacturing better PCFs until 1996 and after that, they became commonplace [49]. Conventional fibers consists of a core and a cladding where core has relatively higher refractive index then the cladding. The light traveling inside the fiber is thus guided by total internal reflection (TIR) mechanism. In photonic crystal fibers, there are two mechanisms to guide light, depending on the fiber geometry. In one type of PCFs, the cladding region consists of air holes, which reduces the effective refractive index of the cladding. In this type of fibers, light is guided by TIR, as in conventional fibers [50]. In the second type, the photonic crystal structure in the cladding is arranged in such a manner that, light is guided inside the core due to the introduced photonic band gap (PBG). In this type of PCFs, core can be made of a material having a lower refractive index than the cladding; the core can even be hollow [51]. SC generation is widely studied in the solid core - air hole cladding PCFs due to design flexibility offered by modifying the air hole size and periodicity, thus, the freedom of tailoring the total waveguide dispersion as well as reduced modal area due to tight confinement to core [14].

The dispersion characteristics of a conventional fiber can also be tailored by tapering the fiber. Since tapering also reduces the modal area of the propagating light, nonlinearity is also enhanced. SC generation obtained by tapered Corning SMF-28 and Newport F-SF fibers were reported by Birks for the first time [52], several other demonstrations of tapered silica fibers and PCFs followed [53, 54].

The nonlinear refractive index of silica is relatively low when compared to some other glasses such as lead-silicate glasses, bismite glasses or chalcogenides. Fibers made of such glasses can be attractive to obtain wider spectra by using

lower power pump lasers. Several examples from the literature for SC generation using highly nonlinear glass fibers are given in references [55, 56, 15]

SC generation was obtained from planar waveguides as well. Planar geometries have the advantage of low fabrication cost and integrability to chip based applications. The total dispersion of the waveguide can also be tailored by waveguide design. Until now, experiments were conducted for silicon [57] and chalcogenide [58, 59] waveguides.

3.2 Description of The Fiber

Chalcogenide glasses consist of a chalcogen element; Se, S, Te and other elements such as As, Ge, Ga, In, Sb. Such glasses have relatively high linear ($\sim$2-3.5) and nonlinear ($\sim$100-9000$\times 10^{20}$ m^2/W) refractive indices. They are particularly suitable for applications in the infrared region, due to their wide transparency region extending between 0.7 μm to 16 μm. Also, ZDW of bulk chalcogenide glasses usually lie in the mid-IR region [33].

In our experiments, we used $\sim$5 mm long and $\sim$7 cm long nanostructured chalcogenide fibers. Our aim was to observe spectral broadening in the mid infrared region where material dispersion is lower. Experiments were conducted at 1.5 μm and 2 μm pump wavelengths.

The fiber used in the experiments was fabricated with the recipe in reference [60]: 25 mm thick cylindrical preform, consisting of 10 mm thick As_2Se_3 rod and layers of 75 μm thick polyethersulfone (PES) film which is rolled onto it was consolidated and drawn to 750 μm thick fibers. Then they were placed around another 9 mm thick As_2Se_3 rod in four concentric rings. PES was rolled over this structure as a protective cladding and 23 mm thick preform was obtained, and drawn into a fiber having an outer diameter of $\sim$830 μm. The obtained fiber was

placed inside a hollow core PES fiber having outer diameter of 3.1 mm. Additional PES film was rolled onto the fiber; consolidation and fiber drawing were performed to obtain a fiber having ∼6 μm diameter As_2Se_3 core. The concentric rings of As_2Se_3 around the core have structures with 200 nm diameter. The final diameter of the region, core + rings is ∼10 μm and the total diameter of the fiber is 800 μm [60]. The fiber drawing steps are summarized in Figure 3.2. Scanning electron microscope (SEM) image of the fiber can be seen in Figure 3.3.

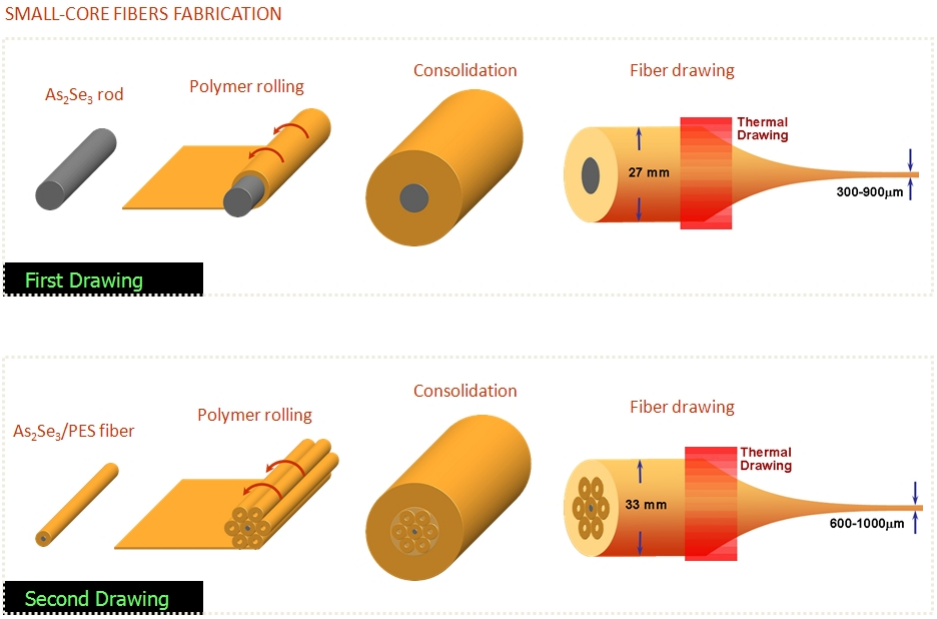

Figure 3.2: The drawing steps of the nanostructured As_2Se_3 fiber.

The material dispersion of As_2Se_3 was calculated using the ellipsometric measurement taken by J.A. Woollam Vis-NIR Ellipsometer System and is given in Figure 3.4. The material dispersion was then calculated by fitting the obtained ellipsometer data into Sellmeier equation:

$$n^2 = 1 + \frac{A_1\lambda^2}{\lambda^2 - C_1} + \frac{A_2\lambda^2}{\lambda^2 - C_2} \tag{3.1}$$

and using the dispersion relation:

$$D = -\frac{\lambda}{c}\frac{d^2n}{d\lambda^2} \tag{3.2}$$

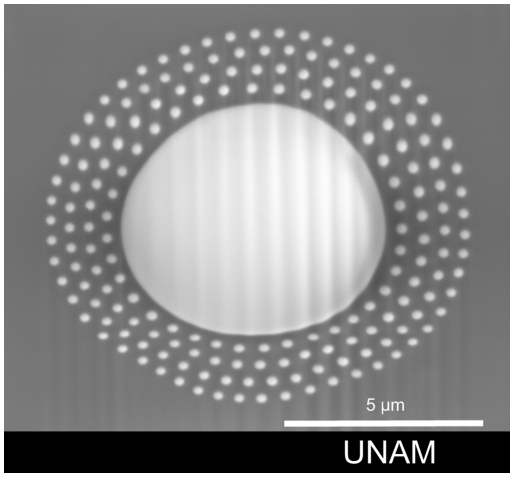

Figure 3.3: The nanostructured chalcogenide fiber used in the experiments.

The obtained Sellmeier coefficients for As_2Se_3 are:

A_1=4.17818 C_1=0.00706

A_2=1.96725 C_2=0.25431

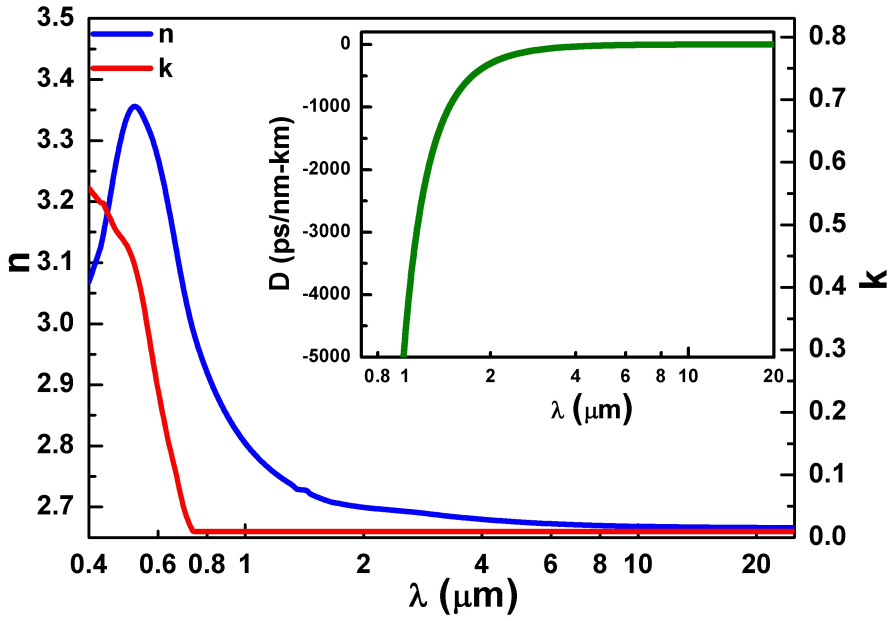

Figure 3.4: The measured refractive index, extinction coefficient and the calculated material dispersion for As_2Se_3.

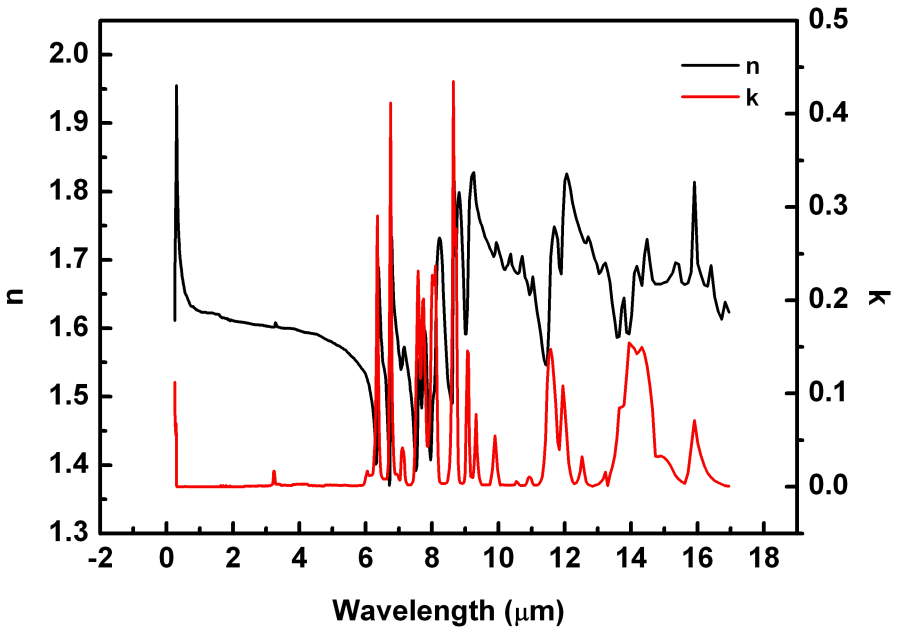

Figure 3.5: The measured refractive index and the extinction coefficient for PES.

The total chromatic dispersion of the nanostructured fiber was also calculated and compared to the material dispersion of As_2Se_3. For this purpose, the effective refractive index of the fiber for a wavelength range were obtained using BeamPROP^{TM} software package of RSoft Photonics Suite. In the simulations, the refractive index of PES was taken to be constant at 1.65 and the refractive index of the As_2Se_3 is defined via the obtained Sellmeier coefficients for the bulk material. The absorption of As_2Se_3 and PES were ignored.

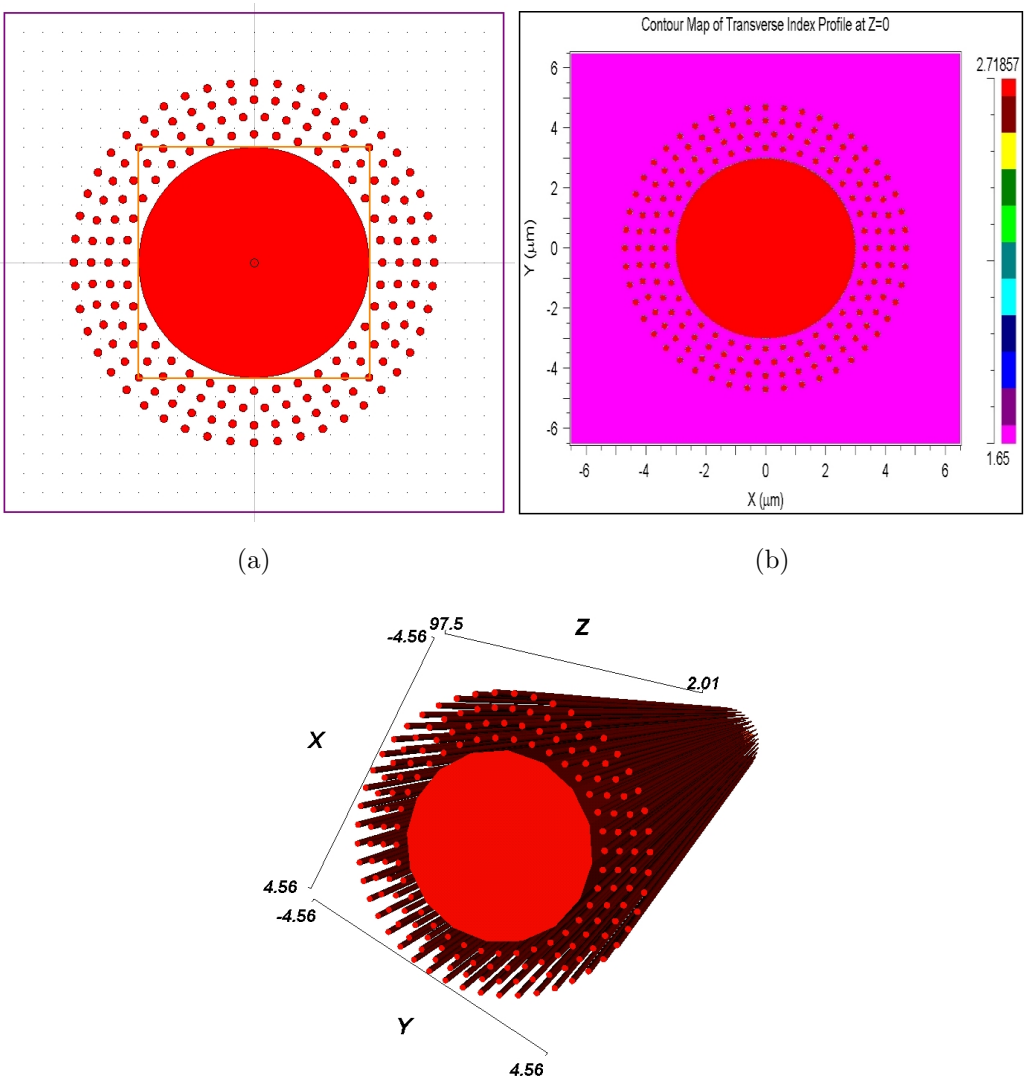

Figure 3.6: (a) The fiber created in RSoft CAD Environment^{TM} for effective refractive index calculation. (b) The material refractive index profile of the nanostructured fiber calculated at 1.55 μm wavelength.(c) 3D image of the nanostructured fiber.

The total chromatic dispersion was calculated by fitting the wavelength dependency of the obtained effective refractive index into the Sellmeier equation. The acquired Sellmeier coefficients for the nanostructured As_2Se_3 fiber are as

follows:

A_1=2.30021 C_1=0.235

A_2=3.83693 C_2=2.5403×10^{-16}

A_3=4.06348 C_3=300

Figure 3.7 compares the total chromatic dispersion of the nanostructured fiber to the material dispersion of As_2Se_3. The zero dispersion wavelength (ZDW) of the fiber was calculated to be at 3.18 μm.

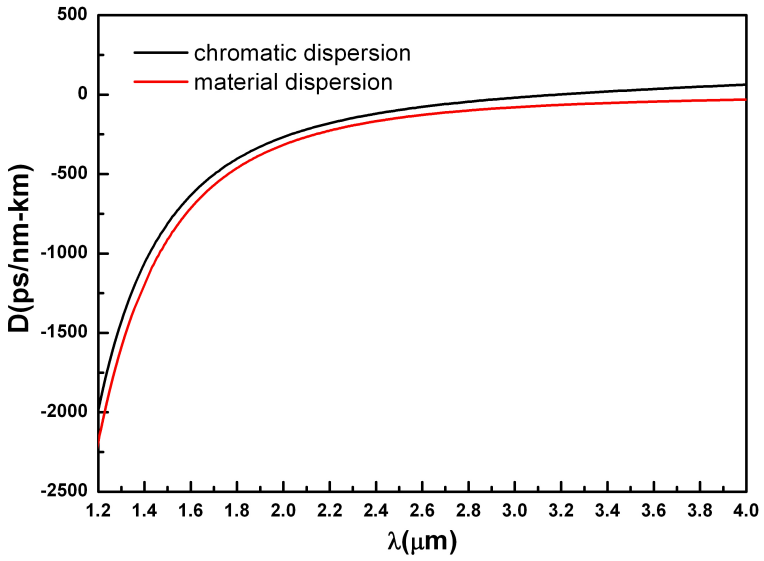

Figure 3.7: The total chromatic dispersion of the nanostructured fiber compared to the material dispersion of As_2Se_3.

Before making the measurements, fibers were polished in order to achieve a better light coupling into and out of the fiber. The polishing was made by hand for the 7 cm long As_2Se_3 fiber and was made using FEI Nova NanoLab 600i focused ion beam (FIB) system for the 5 mm long As_2Se_3 fiber. For polishing by hand, 5 μm, 3 μm, 1 μm, 0.3 μm and 0.5 μm grain size polishing films were used. For the polishing made by FIB, first, fibers were cleaved diagonally by Leica microtome. In addition, an initial flattening of the region, that is to be

polished by FIB was ensured with the same instrument. The reason for diagonal cleaving was to reduce the area of the fiber where the input laser focuses. This was desired due to the fact that when intense laser beam falls on to the PES cladding, the fiber gets burnt. If we could get rid of the PES at the focal area, we could couple more light to the fiber without burning it. Our initial aim was to cleave the fiber diagonally until the core of the fiber. Moreover, polishing and cleaving by microtome before FIB speeds up the FIB etching process.

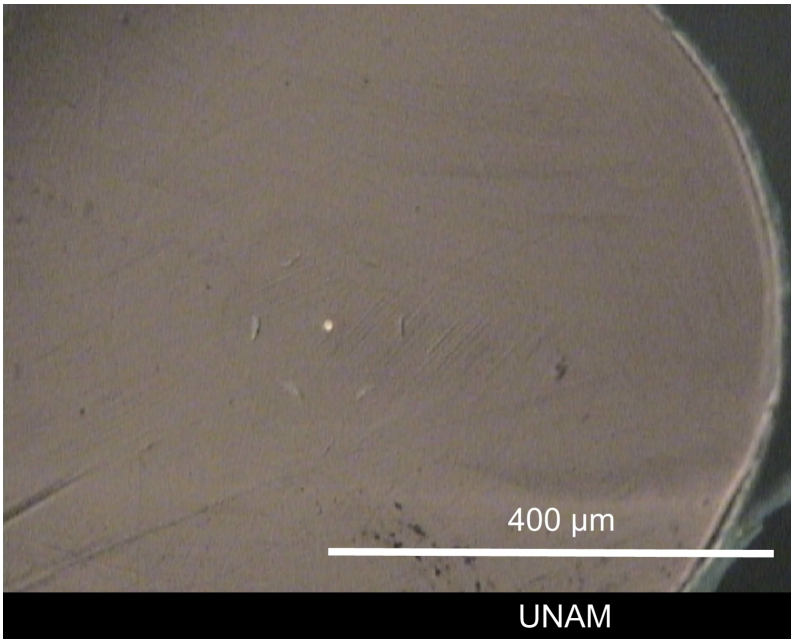

Figure 3.8: Optical microscope image of the fiber after polishing by hand using polishing films.

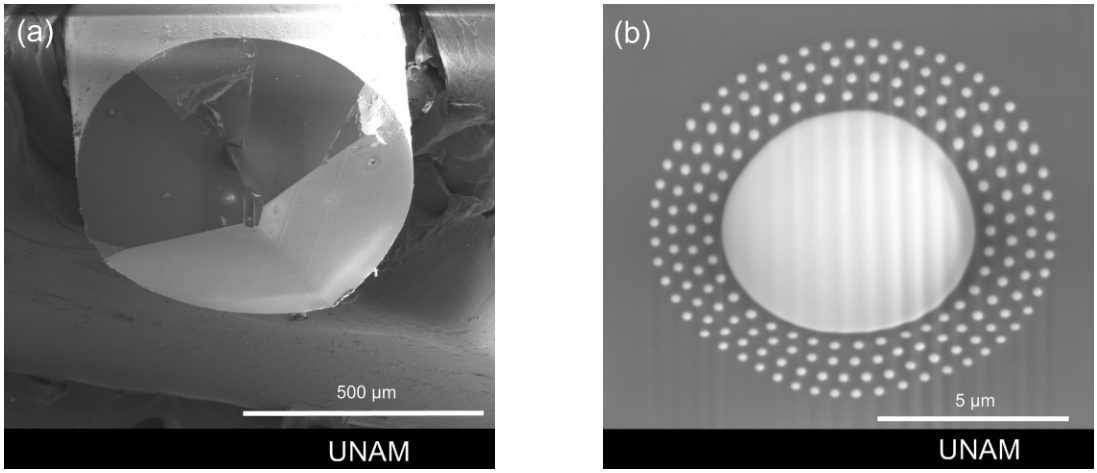

Figure 3.9: (a) SEM image of the fiber after being cleaved and flattened by microtome. (b) SEM image of the fiber's core area after being polished by FIB.

3.3 Numerical Simulations for The Fiber

Nonlinear Schrödinger equation (NLSE) governs the propagation of pulses in a fiber. It can be solved using several numerical methods, since analytical solution is not always available. Split-step Fourier algorithm is an example of such methods. Basically, it is built on the assumption that, when a pulse propagates a small distance h, the effects of dispersion and nonlinearity can be pretended to act independently [31]. In this thesis, a split-step Fourier algorithm, was employed to have an idea on the spectral and temporal broadening in the pulse propagating in a chalcogenide fiber and to observe the effects of dispersion and nonlinearity acting together.

The starting point is the NLSE:

$$\frac{\partial A}{\partial z} + \frac{\alpha}{2}A + \frac{i\beta_2}{2}\frac{\partial^2 A}{\partial T^2} = i\gamma|A|^2 A \tag{3.3}$$

where the α term represents the attenuation in the fiber, the β_2 term represents the chromatic dispersion and the γ term represents the nonlinearities. Eq.(3.3)

can be written as:

$$\frac{\partial A}{\partial z} = \widehat{D}A + \widehat{N}A \tag{3.4}$$

with $\widehat{D} = -\alpha/2 - (i\beta_2/2)(\partial^2/\partial T^2)$ being the dispersion operator and $\widehat{N} = i\gamma|A|^2$ being the nonlinear operator.

The fiber length is divided into small distances, "h". When the pulse propagates through each "h", first, $\widehat{N}$ acts on the pulse, the resulting pulse is transferred to Fourier domain and $\widehat{D}(i\omega)$ acts on the pulse in the Fourier domain; finally, inverse Fourier transform is taken to obtain the resulting pulse in time domain. This procedure is consecutively repeated for each "h" throughout the fiber:

$$A(z+h,T) = F^{-1}\{e^{h\left(\frac{-\alpha}{2}+\frac{i\beta_2}{2}\omega^2\right)}F\{e^{hi\gamma|A|^2}A(z,T)\}\} \tag{3.5}$$

where F represents the Fourier transform and F^{-1} represents the inverse Fourier transform respectively.

The simulations were conducted for a pulse having 150 fs pulse duration, 1.45 μm central wavelength, at varying peak powers of 835 W, 8350 W and 16700 W. The medium was taken to be As_2Se_3 with nonlinear refractive index coefficient, n_2=1250×10^{-20} m^2/W. Dispersion parameter was assumed to be constant at, D= -1000 ps/nm/km. The material dispersion at the central wavelength and an attenuation of -200 dB/m was included. The diameter of the simulated fiber was taken to be 9 μm without considering the PES cladding or the nanostructures around the core. The step size, "h" was 100 μm and the simulated fiber length was 5 cm.

From the simulation results are presented in Figure 3.10, it can be seen that the spectral broadening gets limited after propagating a small distance inside the structure. This results from the large dispersion in the system. After a small propagation distance, the pulse gets broadened in time domain and the peak power is reduced, decreasing the effect of nonlinearity. Also note that, the amount of both temporal and spectral broadening increases with increasing

pump power. The reason is that, as the pump power is increased nonlinearity is enhanced as well, creating more frequency components, shifted towards red near the leading edge and towards blue near the trailing edge of the pulse. This, in turn leads to a larger pulse duration since red components travel faster than the blue ones in normal GVD regime [31].

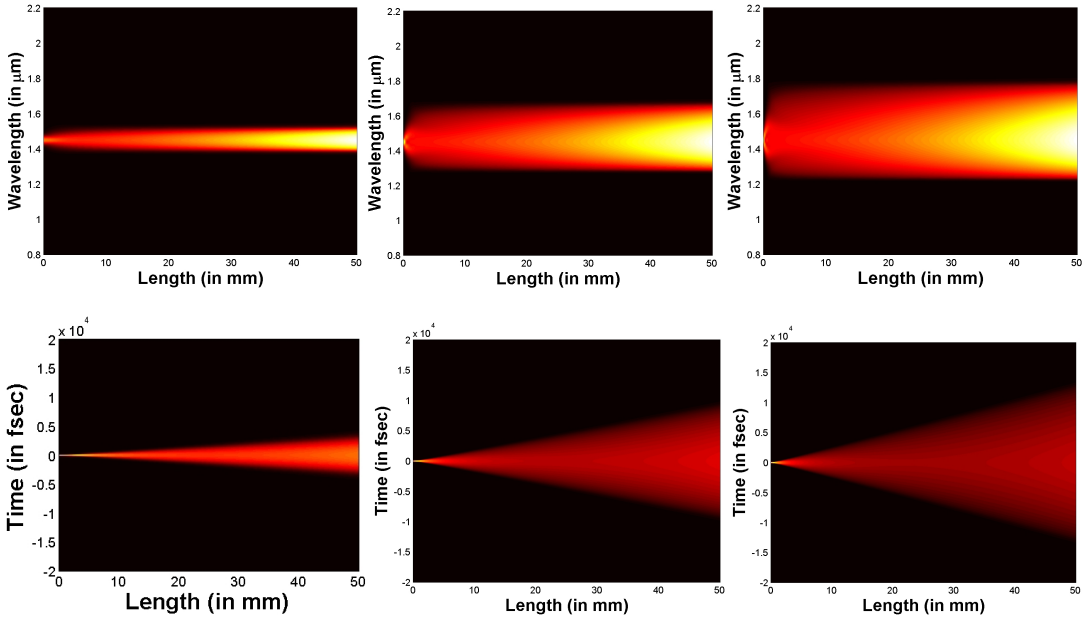

Figure 3.10: Simulation results for peak powers of 835 W (a), 8350 W (b) and 16700 W (c).

3.4 Experimental Setup

As the pump laser, Spectra Physics OPA-800C laser system was used. This system consists of five lasers which are pumping and seeding each other. To follow their theory of operation more easily, they will be referred with their company-given names, and explained in the order of Millennia, Tsunami, Empower, Spitfire and OPA.

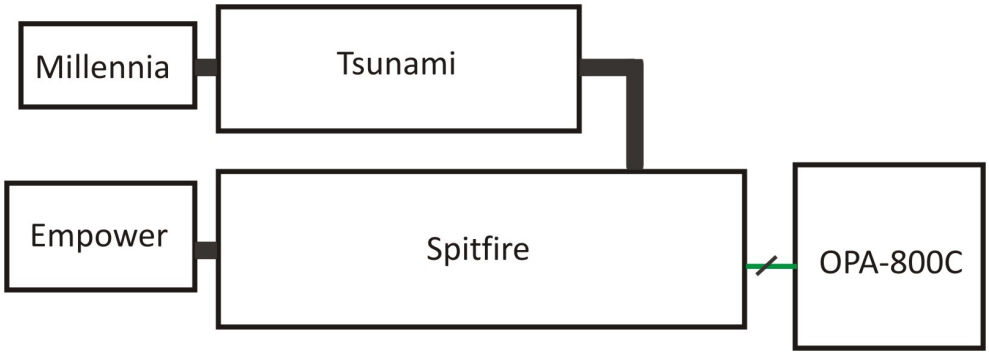

(a)

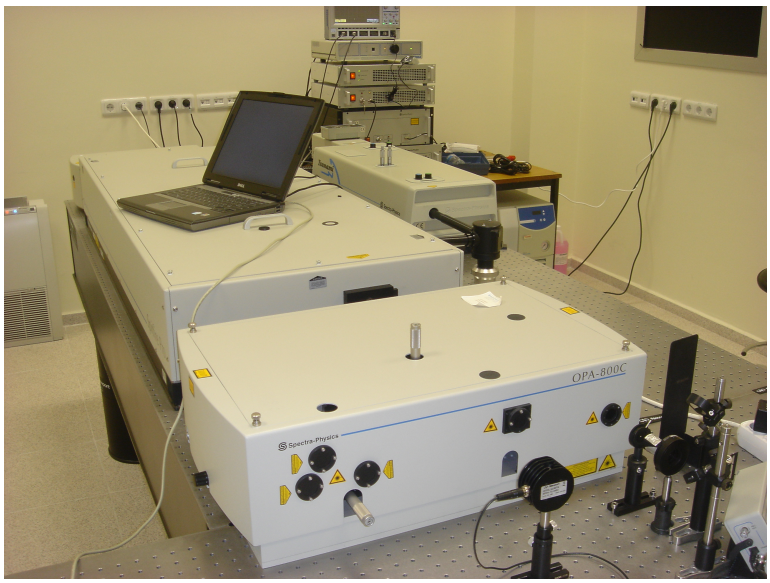

(b)

Figure 3.11: (a) Schematic drawing of UNAM OPA system. (b) The photograph of the OPA system.

Millennia is a frequency-doubled, continuous-wave visible laser, pumped by a fiber coupled diode laser at 800 nm wavelength. The optical cavity of Millennia is an X-cavity resonator where the active medium is Nd:YVO_4 crystal emitting light at 1064 nm wavelength. This light is then frequency doubled in lithium triborate (LBO) crystal to provide a CW output at 532 nm [61].

Light coming from the Millennia enters Tsunami, which is a regeneratively mode-locked Ti:Sapphire laser. In regenerative modelocking, an acousto-optic modulator (AOM) is employed and driven by an RF signal that is directly derived

from the laser cavity. By this method, the RF drive frequency always matches the laser repetition rate. The CW laser entering the Tsunami from Millennia is thus converted to 120 fs pulses at 800 nm wavelength with 80 MHz repetition rate [62].

Empower is an intracavity-doubled, Q-switched Nd:YLF laser that produces pulses at 527 nm wavelength with 1 kHz repetition rate. The active medium, Nd:YLF crystal emits light at 1053 nm wavelength, which is frequency-doubled by an LBO crystal to 527 nm. Q-switching is achieved by employing AOM which enables production of high energy pulses with time durations ∼100 ns and average power levels of 20 W [63].

Spitfire is a Ti:Sapphire regenerative amplifier system that is employed to amplify the pulses produced by Tsunami by a technique called Chirped Pulse Amplification (CPA). The incoming pulses are temporally stretched using a diffraction grating and mirrors and are amplified inside a resonant cavity where the active medium is a Ti:Sapphire crystal. The initial temporal stretching reduces the peak power of incoming pulses which is a crucial step to avoid damaging the crystal and optics. Finally, the amplified pulses are compressed to the desired pulse duration using a similar scheme of diffraction grating and mirrors. In this amplification process, Empower acts as pump and Tsunami acts as seed laser for the Spitfire. The Spitfire output has ∼120 fs pulse duration at 800 nm wavelength with an average power level of 3W. As realized, the peak power of pulses is ∼25 GW showing an enormous amplification as compared to ∼120 kW peak power pulses of Tsunami [64].

OPA-800C is the optical parametric amplifier used in the system that is pumped by the Spitfire giving an output of signal or idler. In an optical parametric amplification process, a high energy pump beam amplifies the low energy seed beam inside a nonlinear crystal. In OPA-800C, a portion of the pump beam

is used to create white light, which provides the seed pulse for parametric amplification. The signal and idler waves are created and amplified in the Beta-Barium Borate (BBO) crystal and the wavelength tuning is achieved by changing the phase-matching angle of the BBO crystal. The available signal wavelengths are between 1.1 μm and 1.6 μm while the available idler wavelengths are between 1.6 μm and 3 μm. Using additional optics, such as second harmonic generation, fourth harmonic generation, sum frequency mixing and difference frequency mixing crystals, a wavelength range extending from 300 nm to 10 μm can be obtained as output [65].

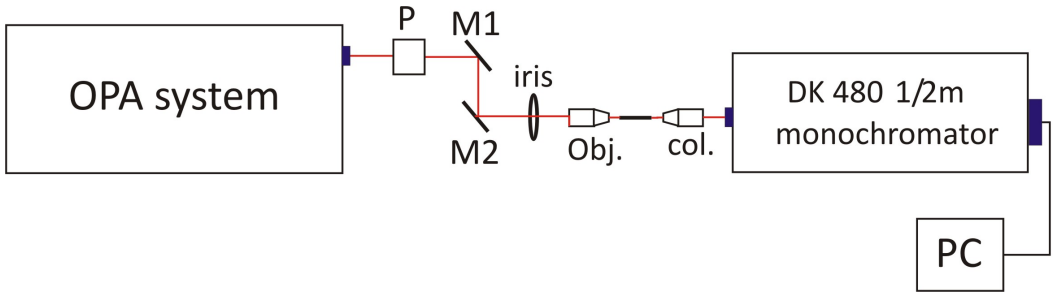

Figure 3.12: The schematic of the experimental setup.

The pulse coming from the OPA enters a Glan-Thompson prism, represented in Figure 3.12, as "P". Glan-Thompson prism is a polarizing prism, from which p-polarized light is reflected and s-polarized light is transmitted. Since the output of OPA is polarized, by rotating the Glan-Thompson prism, the amount of light that is transmitted can be changed. In the setup, the Glan-Thompson prism, together with the iris, was used to adjust the power of light that enters the fiber. After Glan-Thompson prism, light was directed to the iris by the mirrors, M1 and M2. After the iris, light was focused to the entrance of fiber by a 20X microscope objective. At this point, the fiber was intentionally placed further away from the working distance of the objective to lower the pump intensity thereby avoid damaging its end due to intense radiation. The light exiting the

fiber is collimated by a custom made collimator (Spectral Products) and enters 1/2 m monochromator (Spectral Products; Model: DK-480).

The monochromator is a Czerny-Turner type monochromator whose diagram is given in Figure 3.13. The light enters the monochromator from the entrance slit and is collimated at the collimating mirror, C. The collimated light hits the diffraction grating, which disperses different wavelengths at different angles in the plane of incidence. The focusing mirror, E collects the light from the grating and images to distinct positions near the exit slit [66]. A detector is placed at the exit slit, thereby as the grating rotates, the wavelength exiting the slit is changed and the intensity for each different wavelength is recorded.

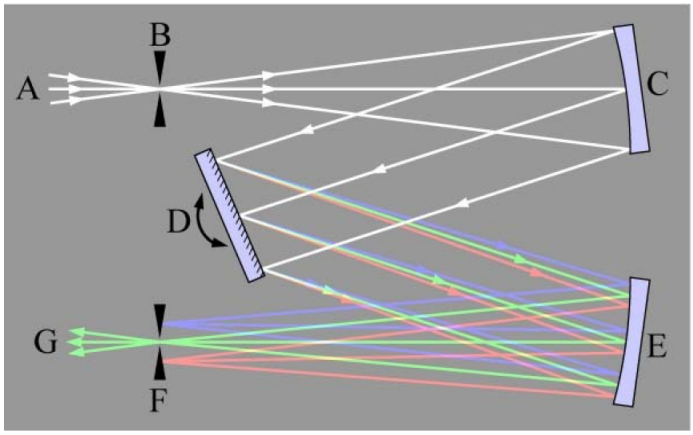

Figure 3.13: The schematic of a Czerny-Turner monochromator. Adapted from Reference [66]

3.5 Measurements and Results

Measurements were taken with the OPA system at 1.5 and 2 μm wavelengths with 150 fs pulses having 1 kHz repetition rate. The aim was to investigate the spectral broadening inside the nanostructured chalcogenide fibers as a proof of principle.

To track experimental findings more easily, measurement results will be systematically presented for each wavelength, fiber type and fiber length respectively.

3.5.1 1500 nm central wavelength

For the experiments conducted at 1.5 μm central wavelength, a thermoelectrically cooled InGaAs PIN photodiode was used as the detector. The measurements were taken from 7 cm and 5 mm long As_2Se_3 core PES cladding fibers, as well as $\sim$5 cm long PES fiber for comparison. The measurements are taken from a 7 cm long nanostructured As_2Se_3 core PES cladding fiber, a 5 mm long nanostructured As_2Se_3 core PES cladding fiber and a 5 cm long PES fiber for comparison.

7 cm long nanostructured As_2Se_3 fiber:

In Figure 3.14, the spectral response of the fiber for 0.32 mW, 2 mW, 15 mW and 21.2 mW average input powers are given. The laser light was not tightly focused to the core of fiber to prevent damaging of its end. Instead, it was placed 1.75 mm further away from the working distance of the microscope objective, maintaining a focal area with $\sim$1.53 mm diameter, as calculated from the numerical aperture of the objective, which is 0.4. We expect that nonlinear effects take place at the core of the fiber, and the contribution of cladding would be very small, if there is any at all.

1 mW average power corresponds to:

$$P_0 = \frac{P_{average}}{repetition\ rate \times pulse\ duration} = \frac{1 \times 10^{-3}}{1000 \times 150 \times 10^{-15}} = 6.67MW \tag{3.6}$$

Since the nonlinear contribution was assumed to come from the core of the fiber, it is important to know the peak power at the core. In described experimental

configuration, some portion of the light did not enter the fiber, since it was defocused to an area larger than the fiber end. Similarly, even smaller part of light enters the fiber core, which has ∼6 μm diameter. Assuming the pulse has uniform intensity distribution in space, the peak power at the core was calculated as:

$$P_{core} = \frac{P_{average} \times (core\ diameter)^2}{(beam\ diameter)^2 \times repetition\ rate \times pulse\ duration} \tag{3.7}$$

which yields a peak power of 103 W at the core for 1 mW average input power.

In Figure 3.14 the spectral broadening from 7 cm long As_2Se_3 fiber is given in terms of peak power levels. As expected, the spectral broadening increased as the peak power was intensified. When looking at the spectral bandwidth at each power level, we defined a standard reference level as 20% of peak to noise difference above the noise level. Since we compared fibers of different lengths and materials, this is a good way to keep a reasonable and consistent reference level for characterizing the spectral broadening.

In Figure 3.14, the noise level was taken from -61.78 dBm; the defined reference level for 7 cm long nanostructured chalcogenide fiber with input peak powers, P_{core}= 33 W, 205 W, 1539 W and 2174 W yielded a spectral broadening of; 79.1 nm, 147.3 nm, 334.9 nm and 382.8 nm respectively.

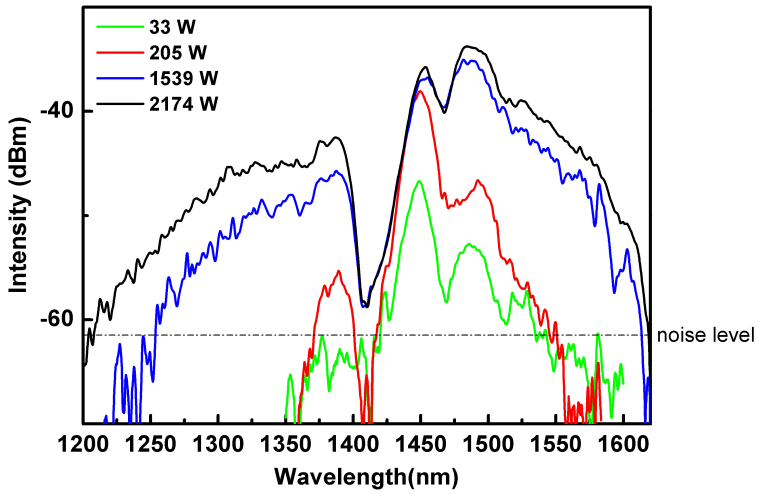

Figure 3.14: The broadening at the end of 7 cm long nanostructured As_2Se_3 fiber at various peak powers.

Figure 3.15 compares the response of nonlinear fiber with the pump laser at similar power level exiting the fiber. Note that the central wavelengths of measurements were slightly different which we believe to be due to slight shift in the OPA alignment. Nevertheless, this should still give an idea. The noise level for the monochromator is -36.9 dBm. If we look from the reference level, the spectral bandwidth was found to be 67.9 nm whereas the same quantity for a nonlinear fiber was realized as 383 nm, demonstrating the effect of nonlinearity existing in the fiber.

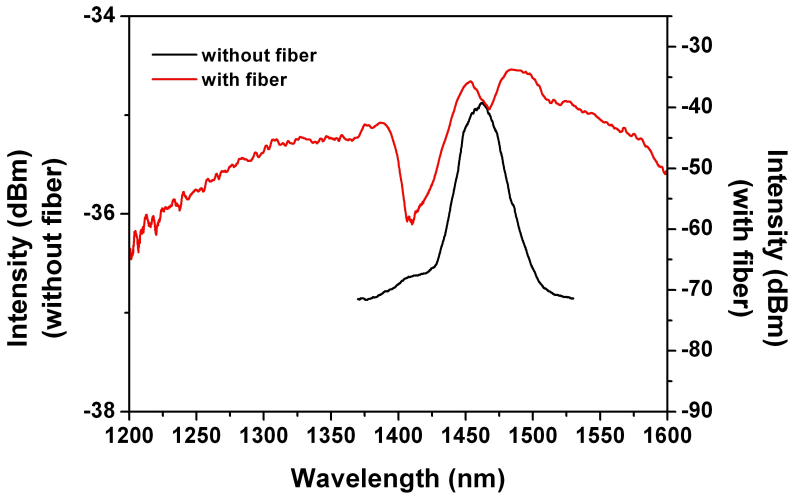

Figure 3.15: Comparison of the spectrum at the end of 7 cm long nanostructured As_2Se_3 fiber with the pump light.

5 mm long nanostructured As_2Se_3 fiber:

Another set of measurements was taken from a 5 mm long nanostructured As_2Se_3 fiber. At this time, the sample was placed 1.3 mm away from the working distance of microscope objective, causing the light to focus to an area with a diameter of 1.13 mm. The obtained results for 60 W, 373 W and 2636 W input peak power levels at the core, were given in Figure 3.16. As expected, the spectral broadening increased with elevated peak power as: 72.5 nm, 102.5 nm and 172.5 nm respectively from the reference level.

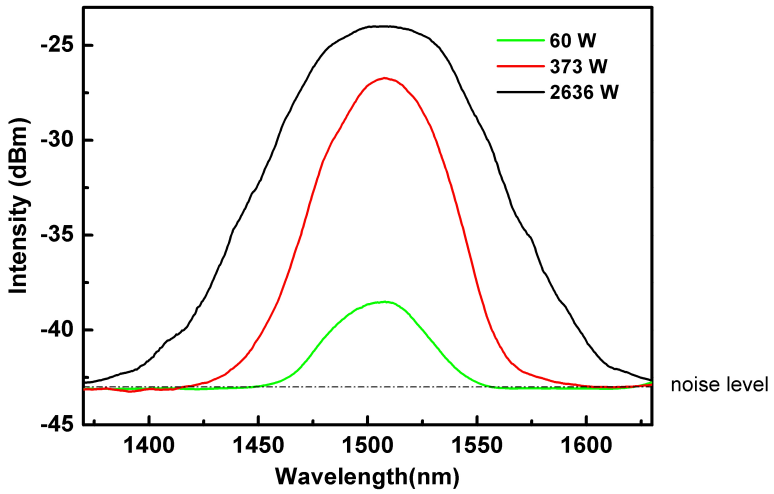

Figure 3.16: The spectral broadening at the end of 5 mm long nanostructured As_2Se_3 fiber for various peak powers.

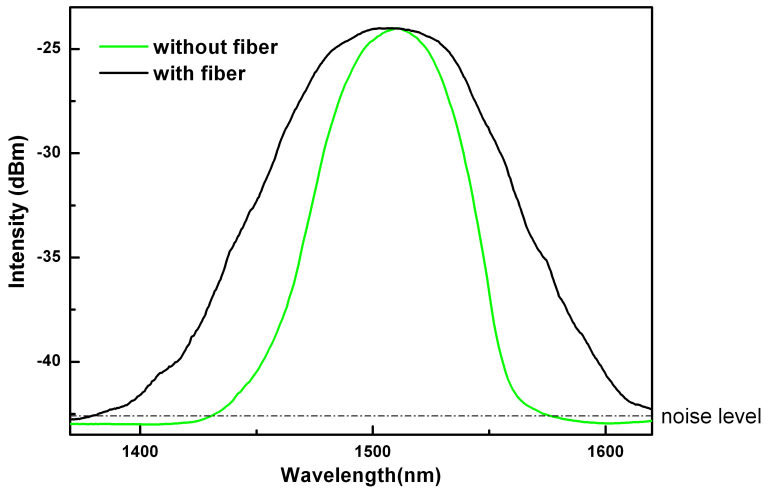

Figure 3.17: The comparison of pump laser spectrum with 5 mm long nanostructured As_2Se_3 fiber output.

Figure 3.17 compares the spectra of pump laser with 5 mm long As_2Se_3 fiber output. From the reference level the pump laser bandwidth was 95 nm whereas the same quantity for the nonlinear fiber was 173 nm showing a moderate broadening.

5 cm long PES fiber:

It was assumed that the PES cladding makes no contribution to the spectral broadening inside the fiber. To test this, a PES fiber of $\sim$300 μm diameter was excited at 1520 nm central wavelength with the same experimental configuration yielding 470 kW peak power for 1 mW average power on the fiber front due to increased area.

The spectrum was inspected at various input power levels where the spectral bandwidth was recorded as 61 nm, 81.5 nm and 101.5 nm for 150 kW, 940 kW and 2821 kW input powers respectively, demonstrating a very slight broadening. Such an increase, however is not as strong as the effect that we observed in chalcogenide fibers.

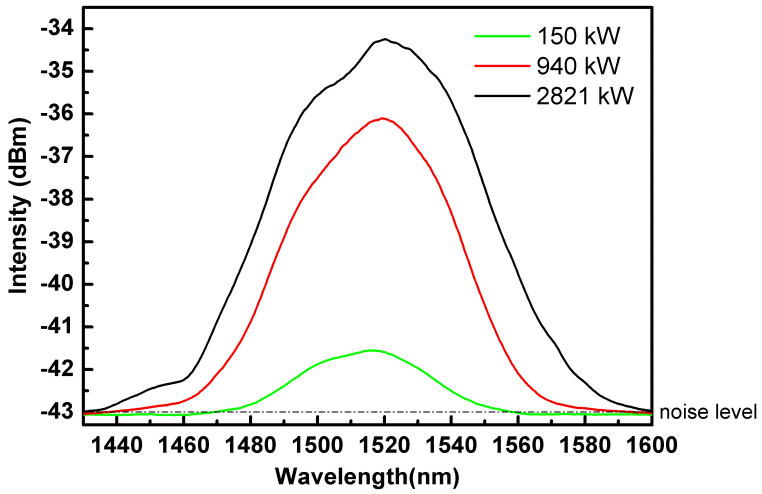

Figure 3.18: The broadening at the end of 5 cm long PES fiber for various input powers.

When the spectral bandwidths for each type of fiber are compared, for the same intensity level, i.e. 6408 W/m^2, it is seen that, 5 mm long chalcogenide fiber has a bandwidth of 152.5 nm; 7 cm long chalcogenide fiber has a bandwidth of 334.9 nm and 5.5 cm long PES fiber has a bandwidth of 101 nm. As can be seen, a substantial broadening occurs in the 7 cm long nanostructured fiber compared to other types at the same power level, verifying the effect of nonlinearity along with the fiber length.

3.5.2 At 2000 nm central wavelength

Measurements at 2000 nm wavelength was also taken for 7 cm and 5 mm long As_2Se_3 as well as 5 cm long PES fibers. They are conducted with a PbS photodetector cooled to -10°C and a lock-in amplifier to increase the signal to noise ratio.

7 cm long nanostructured As_2Se_3 fiber:

In these measurements light was focused to an area of 1.13 mm. The resultant spectra for peak power levels of 111 W, 2343 W were shown in Figure 3.19. The realized bandwidths at the reference level are 152 nm and 281 nm accordingly.

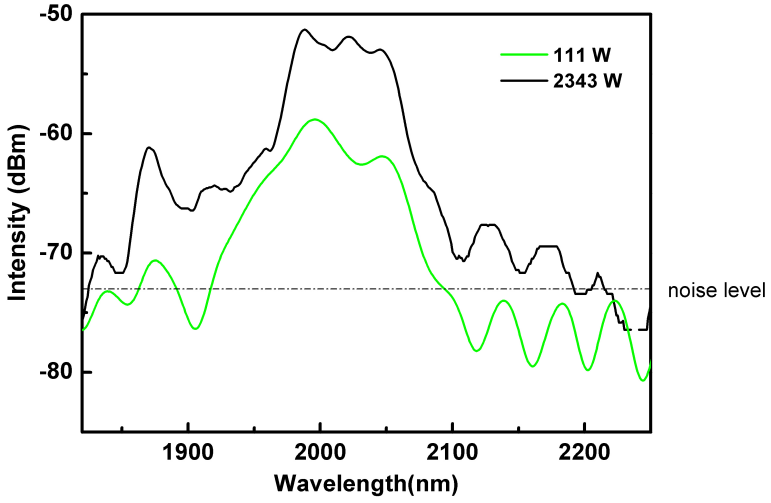

Figure 3.19: The broadening from 7 cm long As_2Se_3 fiber for various input powers at 2000 nm central wavelength.

5 mm long As_2Se_3 fiber:

Same experimental scheme was used as before with input peak powers of 0.5 W, 1 W, 11 W, 111 W, 580 W and 2343 W at the core. The recorded spectral bandwidth from the reference level was then 189 nm, 188 nm, 264 nm, 330 nm, 361 nm, and 455 nm respectively, Figure 3.20.

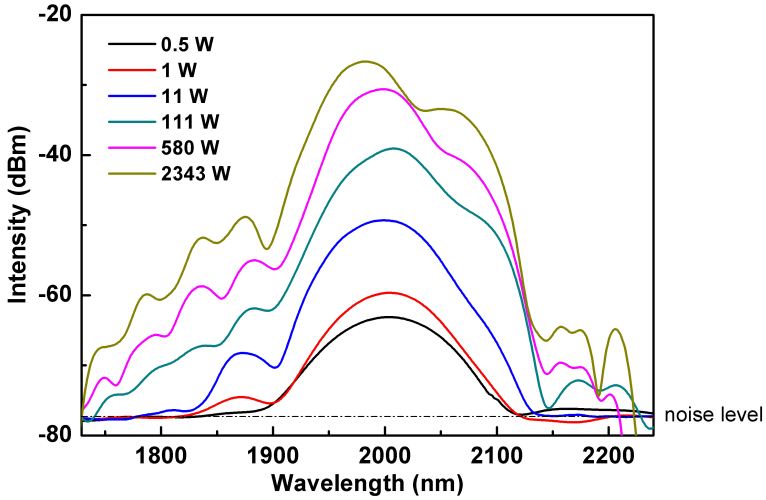

Figure 3.20: The broadening at the end of 5 mm long As_2Se_3 fiber for various input powers at 2000 nm central wavelength.

5 cm long PES fiber:

Measurements were taken for this fiber at the peak power levels of 1463 kW, 2944 kW, and 5904 kW inside the fiber where the measured bandwidths were 93 nm, 99 and 99 nm respectively showing no observable broadening effect at all.

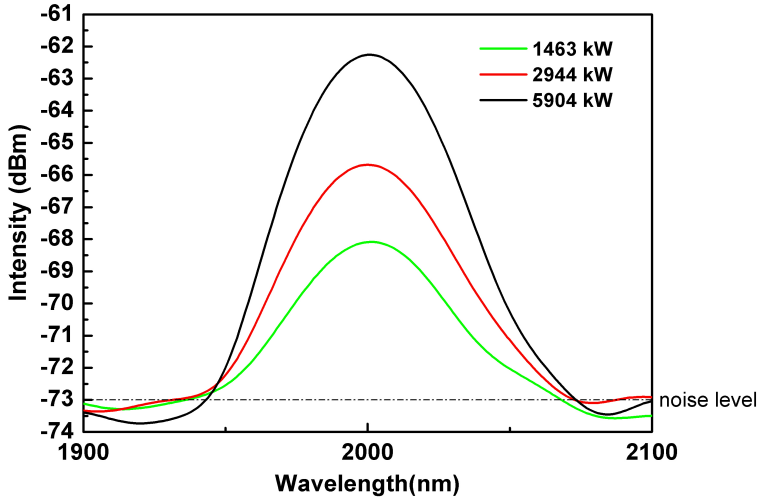

Figure 3.21: The spectrum at the end of 5.5 cm long PES fiber for various input powers at 2000 nm central wavelength.

5 mm long PES fiber:

The fiber is placed 1.3 mm away from the microscope objective as before. The peak power levels for light entering the fiber are calculated and given in Figure 3.22. The spectral bandwidth is: 265 nm for 278 kW; 290 nm for 1463 kW and 313 nm for 5904 kW peak power levels inside the fiber. The spectrum has not changed significantly with increasing power levels, indicating that the nonlinear effects are insignificant. Moreover, in Figure 3.24, it can be seen that the spectra at the end of 5 mm long PES fiber and the monochromator response in the absence of the fibers are very similar. This suggests that the effect comes from the undesired signals at OPA output. Still, to make a healthy comment on the phenomenon, the measurements need to be repeated when the OPA output is filtered.

When compared to PES measurement results at 1500 nm, we observe a difference that no broadening occurs at this wavelength unlike the previous case. Although the reason for such a behavior is unclear there are couple possibilities that can lead to this result. First, it is possible that these are the contributions due to OPA signal, since its spectrum is not pure and has sidebands at either wavelengths, which can be attenuated at 2000 nm since the absorption of PES at this wavelength range is stronger than its absorption at ∼1500 nm. Second possibility is that, indeed there is some nonlinear broadening at 1500 nm, but the same effect do not reveal itself at 2000 nm due to stronger absorption of PES. From our perspective it is difficult to make conclusive remarks on this issue since the effect is not strong enough to differentiate from instrumental artifacts.

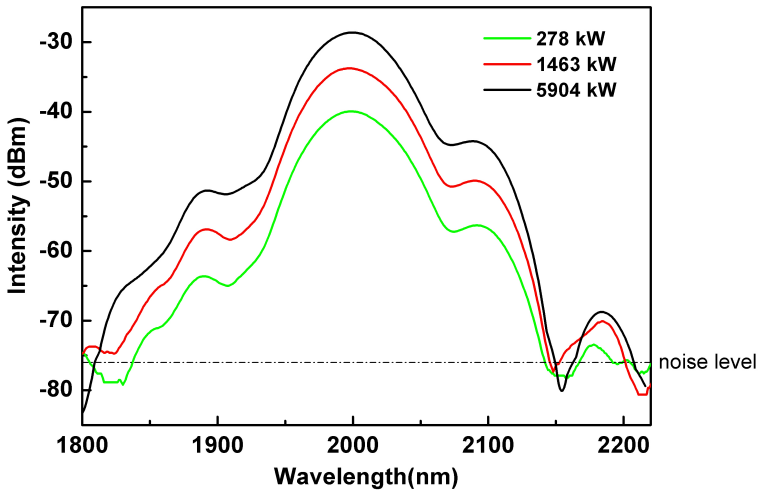

Figure 3.22: The broadening at the end of 5 mm long PES fiber for various input powers at 2000 nm central wavelength.

In Figure 3.23, the spectra at the end of various fiber types are compared for the same intensity level, 10181 W/m^2. The spectral broadening for various fiber types are: 281 nm for long chalcogenide fiber, 455 nm for short chalcogenide fiber, 99 nm for long PES fiber and 313 nm for short PES fiber. If we compare

these results to the bandwidths observed at 1500 nm wavelength which are: 382.8 nm for long chalcogenide fiber, 172.5 nm for short chalcogenide fiber and 141 nm for long PES fiber. These results suggest that, the OPA output is cleaner for 1500 nm wavelength than it is for 2000 nm. Also, the fact that bandwidth for long chalcogenide fiber is narrower than the short one indicates that there is a significant amount of loss inside the fiber at 2000 nm. This suggests that some portion of light with new generated frequencies leaks to cladding layer and gets absorbed by PES which reduces their intensity to noise level, and therefore causes narrowing of the overall bandwidth.

The smallest output power level was observed from the 5 cm long PES fiber, as expected, since the absorption of PES is high in this wavelength region. The spectra of the short chalcogenide fiber and the short PES fiber were very similar. Only an additional broadening was observed inside the chalcogenide fiber. The slightly higher power level of short chalcogenide fiber compared to the short PES fiber most probably results from the fact that more light was coupled to the 800 μm diameter chalcogenide fiber.

In Figure 3.24, the spectra of 5 mm long chalcogenide and PES fiber were compared with the spectrum of pump laser at around power levels exiting the fiber. As can be seen there is no substantial difference, implying that the effect of spectral broadening is weak.

We conclude that nanostructured AS_2Se_3 core, PES cladding fiber shows modest spectral broadening efficiency $\sim$2000 nm wavelength whereas it becomes stronger at $\sim$1500 nm, despite the relatively smaller GVD in the former region. Moreover, using PES as the cladding material is not very efficient for observing nonlinear interactions since it can easily burn due to intense radiation and it is considerably absorbent in the IR region reducing the signal level.

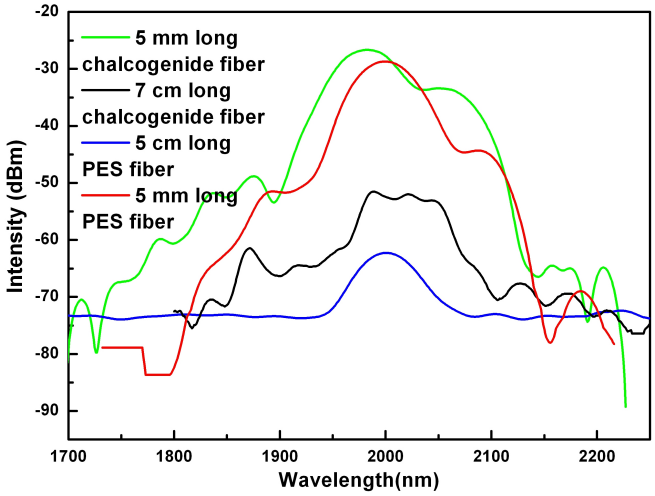

Figure 3.23: Comparison of the spectra of 7 cm long As_2Se_3 fiber, 5 mm long As_2Se_3 fiber; 5 cm long PES fiber and 5 mm long PES fiber.

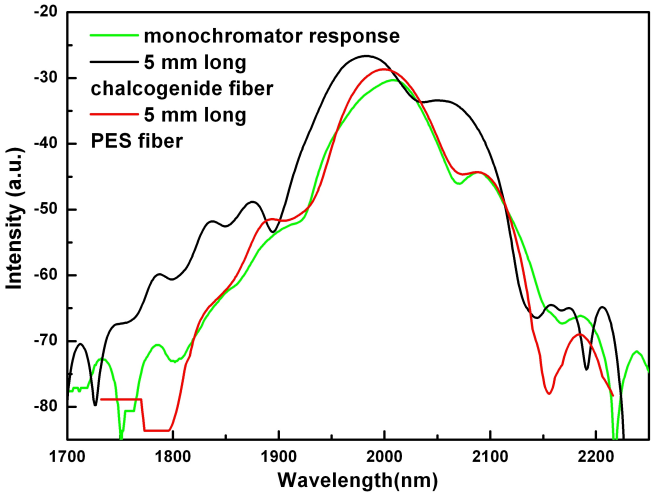

Figure 3.24: Comparison of the spectra of 5 mm long As_2Se_3 fiber; 5 mm long PES fiber and the monochromator response when there is no fiber.

3.6 WGM Microresonators

The whispering gallery mode (WGM) microresonators will be described in more detail in Chapter 4, however, here, only a brief introduction will be made. Whispering Gallery Mode (WGM) Microresonators are structures that confine light in a micron scale area via Total Internal Reflection (TIR) mechanism. Microdisks [67], microspheres [25], microrings [68], microdroplets [69] and microtoroids [27] are examples of such resonators. The importance of WGM microresonators stem from their high quality factors, up to 8×10^9 observed in silica microspheres [70]. Also their small size results in excellent mechanical stability and easy control of resonator parameters [71].

Due to ultrahigh quality factor $\sim10^8$, small mode volume and integrability to chip based applications, microtoroids have drawn much attention from their first demonstration by Armani [27]. It has been employed for demonstrating a broad range of physical phenomena from chemical sensing to cavity quantum electrodynamics [22, 23]. It is also attractive for observing nonlinear optical effects due to ultrahigh quality factor, enabling better confinement thereby increasing the interaction time of light with matter and small mode volume, enhancing the light intensity, consequently nonlinearity [72, 18].

In this study we numerically investigated non-linear interactions occurring in WGM microtoroid resonator which is coated with nonlinear material of As_2Se_3, using FDTD method.

3.7 FDTD Simulations for Nonlinear Effects on Toroidal Microresonator

The simulations were conducted using FullWAVE^{TM} software which was developed by RSoft Photonics Suite. FullWAVE^{TM} uses finite difference time domain (FDTD) algorithm to solve the electromagnetic field in space and time domain. FDTD provides a direct solution to Maxwell's equations and is especially useful when the Beam Propagation Method solutions are not adequate or cannot be applied to the structure geometry. FullWAVE^{TM} program calculates the EM field as a function of time and space, however, by taking the Fourier transform of the obtained time domain result, it also yields field information in frequency domain.[73]

To investigate the spectral response of a microtoroid to incoming electromagnetic field, a two dimensional analogue of a SiO_2 microtoroid coated with As_2Se_3 was created with specifications of 61 μm major diameter, 2 μm minor diameter and 1.5 μm thick As_2Se_3 coating on top.

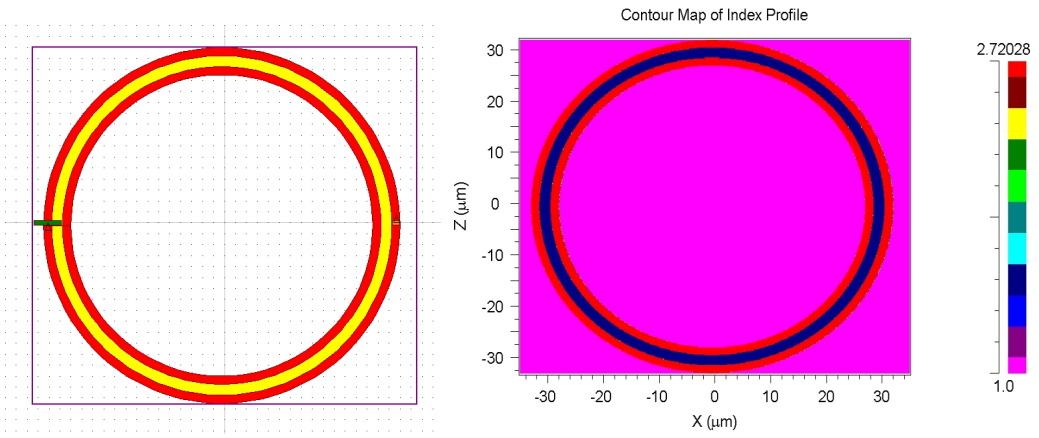

Figure 3.25: (a) The two dimensional toroid analogue that is used in FDTD simulations. (b) The refractive index profile of the structure in (a).

During our simulations, taking the time constraints into account, a stop time of 25000 cT(μm), in FullWAVE units, was used.

For the material dispersion of As_2Se_3, Sellmeier coefficients obtained from the ellipsometer data were employed. The Sellmeier equation is:

$$n^2 = 1 + \frac{A_1\lambda^2}{\lambda^2 - C_1} + \frac{A_2\lambda^2}{\lambda^2 - C_2} \tag{3.8}$$

where the used Sellmeier coefficients are:

A_1=4.17818 C_1=0.00706

A_2=1.96725 C_2=0.25431

The refractive index of the silica layer underneath was taken to be constant as 1.5. During the simulations, several assumptions were made; the absorption of the materials were ignored as well as scattering. The excitation was pulsed with time duration of 152 fs and at 1.5243 μm central wavelength.

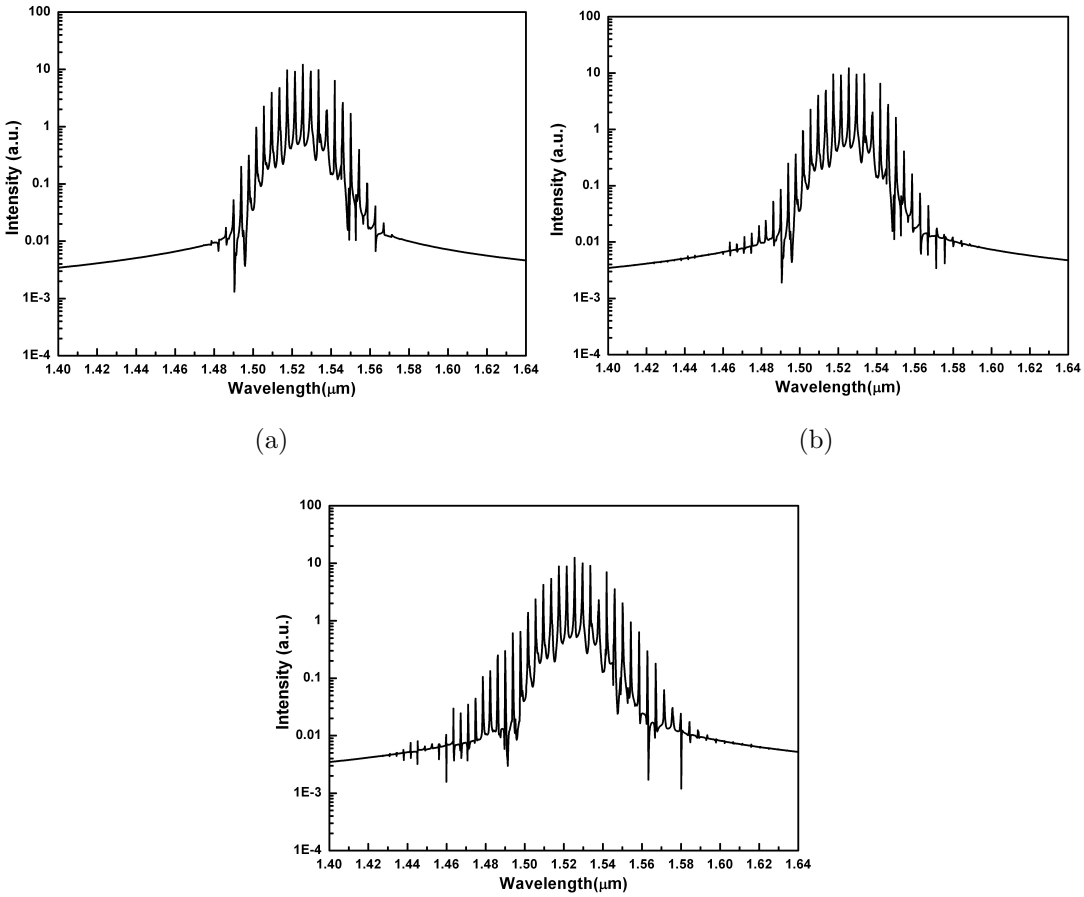

(a) (b)

(c)

Figure 3.26: (a) Simulation results for a linear toroid, i.e. $\chi^{(3)}$=0 is taken in FullWAVE with input peak power, P=10 W. (b) Simulation results for a toroid when nonlinearity of As_2Se_3 is taken into account. $\chi^{(3)}$=931×10^{-13} esu with input power P=2 W. (c) Simulation results for microtoroid when input power, P=10 W. Other parameters are the same as in (b).

From the results, it can be seen that the calculated resonance spectrum of the microstructure gets broader as the input power is increased. Note the observed spectral broadening of ∼100 nm even for a very low peak power level of 10 W, which seems to be promising. We could not succeed in using higher peak powers in the simulation, since it becomes unstable and gives incorrect results. This problem may be avoided by employing a nonlinear saturation coefficient for the material which was not at hand in our case.

Chapter 4

LASING ACTION FROM POLYMER COATED TOROIDAL MICRORESONATOR

4.1 Introduction

WGM resonators were already introduced in Chapter 3. Such cavities with high quality factor maintain narrow resonance linewidths and therefore are attractive for many applications [71, 74, 22]. They can be used as photonic filters in telecommunications [19], also as chemical sensors by monitoring the change in cavity resonances [22]. In addition, enhanced non-linear interactions due to improved confinement properties have been demonstrated [74] along with cavity QED experiments [24] and microlaser applications [20, 75].

High quality factor of WGM resonators lead to reduction of threshold for lasing action. Until now, the highest quality factors have been observed in surface

tension induced microcavities (STIM) due to extreme reduction of scattering centers existing on the structure's surface by reflowing. Common examples of STIMs are microspheres and microtoroids. Although the former usually retain higher quality factors compared to the latter, microtoroids are more advantageous since they can be produced on chip with a more controllable fabrication procedure and their mode volumes are usually much smaller than that of microspheres; a crucial factor for nonlinear applications. Nevertheless, microtoroids still possess Q-factors $\sim 10^8$ which is comparable to that of microspheres and highest Q/V factor of 10^6 $(\lambda/\mathrm{n})^{-3}$ among chip based microresonators [27, 76].

The microtoroids have so far been employed for a variety of purposes including cavity QED experiments [23, 77], optical sensors [22, 78], nonlinear optics [17, 18] and laser action [21, 79, 80].

4.2 π-Conjugated Polymers and DOO-PPV

Two types of chemical bonding, π and σ, are important in determining electronic properties of a polymer. σ bonding is created by the sp^2 hybridized carbon electrons in the plane of a molecule [35], whereas π bonding is formed by the electrons in $2P_z$ orbital perpendicular to molecular plane. Among the two types, σ bonds are the structural glue of polymer chain [35] and have localized electrons; whereas π bond electrons are delocalized over the backbone of the polymer chain and therefore enhance the conduction of charge carriers [81]. Generally, polymers are known to be insulating materials, however, π-conjugated polymers show semiconductor properties since π and σ bonds in the double bond configuration is alternating and therefore creating a band gap between π bonding and π^* antibonding levels which are sometimes also called highest occupied molecular orbital (HOMO) and lowest unoccupied molecular orbital (LUMO) respectively, similar to valence and conduction bands of normal semiconductors. Usually for

conjugated polymers this bandgap is in the range of 1.5-4 eV [81]. With this information given, Poly (dioctyloxy-*p*-phenylene-vinylene) (DOO-PPV) is a π-conjugated polymer with very high quantum efficiency [82] which can show laser action when optically excited. Absorption and photoluminescence spectra of this polymer is given in Figure 4.1.

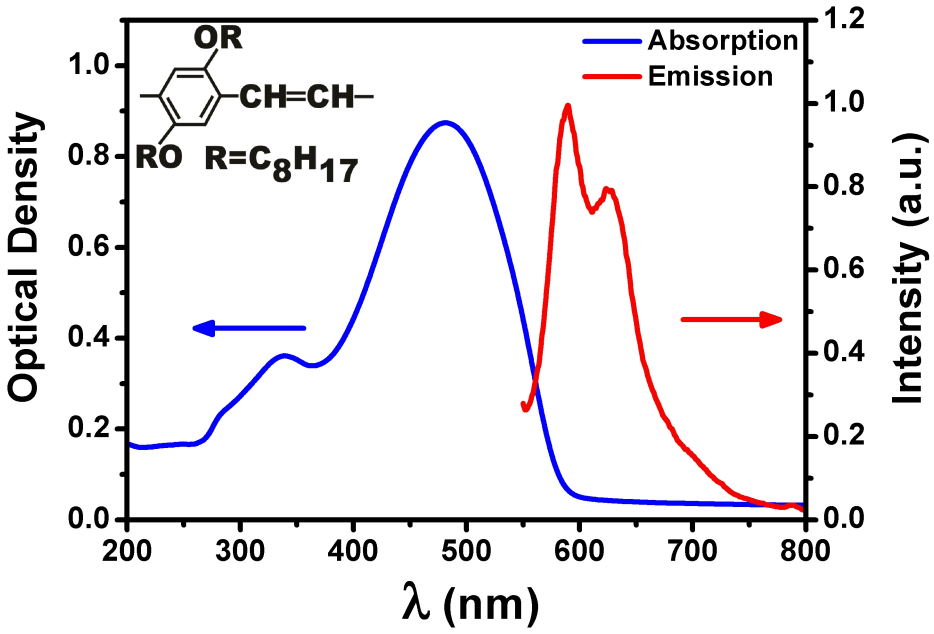

Figure 4.1: The absorption and photoluminescence from DOO-PPV polymer. The data is taken using Cary 100 Bio UV-Vis spectrophotometer. Inset is the structure of DOO-PPV.

The ellipsometer data for the DOO-PPV polymer is also given, Figure 4.2. Here, the extinction coefficient is unexpectedly high, when compared to the absorption data taken by the spectrophotometer. Therefore, the refractive index fit provided here is the combination of the values where k was assumed to be zero (for 600 nm and longer wavelengths) and non-zero (shorter than 600 nm). However the presented k spectrum was obtained by assuming a nonzero k value for the whole spectral region and may not be very accurate for 600 nm and longer wavelengths.

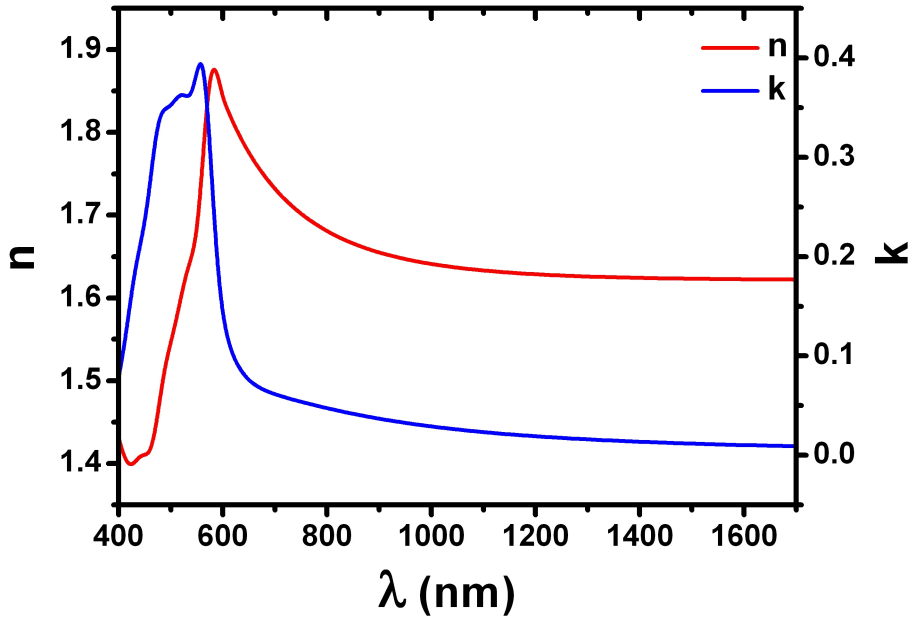

Figure 4.2: The refractive index and extinction coefficient for DOO-PPV polymer.

4.3 Aim and Motivations

Employing WGM microcavities for observation of laser action is very advantageous: since there are no mirrors involved in the cavity, very small and efficient lasers can be obtained. Moreover it is usually important to obtain such microlasers on chip due to a variety of potential applications especially in the area of integrated optics and optical sensing. Therefore the microtoroid, being an on-chip microresonator and having an ultra-high quality factor seems to be the best candidate for such a purpose. However, there is an important drawback of employing a toroidal microcavity, or some other WGM microresonator as the cavity for laser action; the coupling of light in and out of the structure is not easily achieved. The common and simple method of free space excitation is very inefficient for this sort of microlasers, causing an increased lasing threshold. Several efficient methods of coupling the light into the cavity include tapered fiber

coupling [83, 41], prism coupling [70], eroded or side polished fiber coupling [84]. It was demonstrated in the literature that, threshold for a microtoroidal laser cavity, coated with CdSe/ZnS (core/shell) quantum dots, has been reduced by a factor ∼2600 when light is coupled to the cavity with a tapered fiber instead of free space excitation [21].

Our aim in this study is to observe laser action from DOO-PPV coated microtoroid resonator. Despite the fact that free space excitation is inefficient for this purpose, we employed this technique since it is experimentally very easy and demands less technical resources.

4.4 Microtoroid Fabrication

We have used thermally grown SiO_2 on a commercially available Si substrate. It is important to use thermally grown SiO_2 since it maintains less stress compared to oxide films grown using other methods such as PECVD. This fact becomes very critical as the SiO_2 microdisks are undercut; a wavy structure, Figure 4.4, around the rim of cavity is developed due to high residual stress when PECVD grown oxide is used, making it impossible to obtain a smooth toroidal shape by just reflowing the structure with a CO_2 laser. The main fabrication steps of microtoroid are given in Figure 4.3 and the fabrication procedure is as follows:

1. Photolithography: The disk structures, which were designed and produced on a Cr mask before, were transferred to the thermally grown SiO_2 layer by conventional photolithography techniques. For this purpose, AZ 5214 E photoresist, with image reversal capability, was coated on the wafer by spin casting at 5200 rpm. Image reversal was achieved by a special crosslinking agent in the resist formulation which becomes active at temperatures above 110°C in the areas exposed to UV light [85]. The wafer with photoresist was first soft baked at 110°C for 60 seconds to obtain a smoother and cleaner photoresist layer. After the soft

baking, the wafer was exposed to UV light for 40 seconds with the Cr mask on top, using Karl Suss MJB3 Mask Aligner, which utilizes a Hg lamp with i-line at 365 nm. Next, the sample was baked at 110°C for 120 seconds resulting in UV exposed areas to be much less soluble in the developer and also insensitive to light [85]. The sample was then exposed to UV light without a mask, i.e. flood exposure, for 40 seconds, making the previously unexposed areas soluble in the developer. With this manner, reverse of the mask image was attained on the photoresist. Finally, the sample was developed for ∼35 seconds at a AZ 400 K developer prepared with 1:4 developer:water ratio and hard-baked at 110° for 5 minutes for hardening the photoresist.

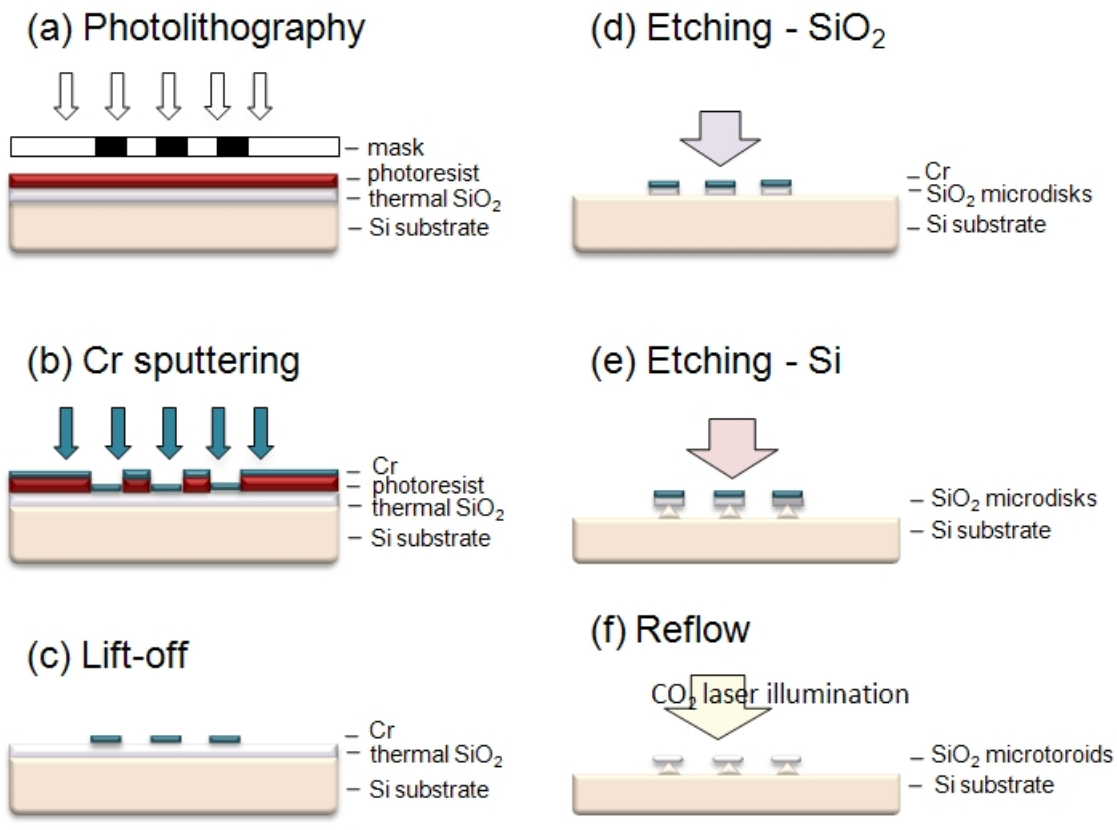

Figure 4.3: Main fabrication steps of the microtoroid cavity.

2. Cr Sputtering and Lift-Off: Chromium was deposited onto the sample after the photolithography process using box coater system. Sputtering was used as the deposition technique since it is faster than evaporation. Chromium target was placed inside the chamber of the box coater and vacuumed. Next, RF plasma was created inside the chamber using Ar gas. Energetic ions created by the plasma remove atoms from the chromium target which then stick to sample on top. Once chromium was deposited, a lift-off process was performed, removing the photoresist as well as the Cr layer on top with acetone. At the end of this step, microdisk structures from Cr metal were obtained on top of the SiO_2 layer. The reason for the use of Cr metal is that it is highly resistive to plasma etching steps followed in the fabrication process unlike the photoresist itself.

3. Etching of SiO_2: The SiO_2 layer was dry etched using Reactive Ion Etcher (RIE) system with the plasma of CHF_3(100 sccm) and O_2(40 sccm) at 100 W RF power and 66 μbar chamber pressure. In this method, a plasma is created inside the vacuum chamber and the reactive gas etches the target material with the help of plasma. Dry etching is usually preferred over wet etching with HF, since it is more controlled and anisotropic, creating smoother structures. The chromium pattern created in the previous steps acted as an etch mask preventing the removal of SiO_2 layer underneath that would eventually become microdisks.

4. Etching of Si: Initially, a wet silicon etchant, KOH was tried for etching the Si substrate. However, since KOH etches Si anisotropically at each crystallographic plane, the resultant pillars had hexagonal shapes, Figure (4.4). This would lead to nonuniform microtoroids after reflow. Therefore, isotropic dry etching was considered. The Si substrate underneath the SiO_2 layer was etched in RIE with SF_6(28 sccm) plasma at 51 W RF power and 100 μbar chamber pressure. This process is highly selective and isotropic, resulting in circular Si pillars holding the SiO_2 microdisks suspended in air. At the end of this step, the residue of Cr layer, that has been used as a mask during dry etching was removed using the Cr etchant CR-7. Finally, we have SiO_2 microdisks suspended

in air on a silicon pillar.

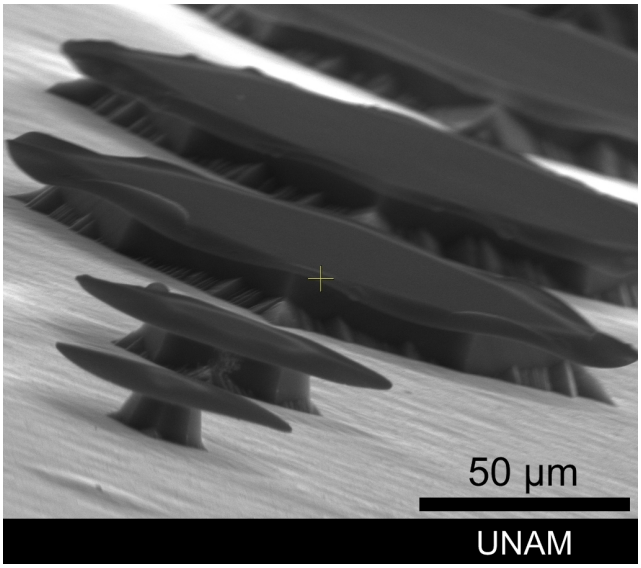

Figure 4.4: The suspended microdisks obtained when SiO_2 is grown using PECVD and Si is etched with KOH.

6. Reflow of The Microdisks: Microdisks were reflown using a CO_2 laser with emission wavelength of 10.6 μm. This step considerably increases the quality factor of microresonators due to the reduced surface roughness on the rim of the microstructures. The absorption coefficient of Si is much less than that of SiO_2 at the wavelength of CO_2 laser. Most of the illuminated power was absorbed by microdisks and not the pillars since Si is transparent in this spectral range whereas silica is highly absorbent. In addition, as the Si has 100 times higher thermal conductivity than silica, the pillar behaved as a heat sink causing the center of microstructure to be relatively cooler with respect to the edges [86]. Consequently, melting due to high temperature only occurred on the rim of the oxide microdisks, yielding the shrinkage of diameter and redefining of the structure's shape to a microtoroid. As the rim diameter contracts, the structure absorbs less amount of optical power and becomes closer to Si pillar, cooling down the microtoroid and eventually stopping the melting process.

Finally, a toroidal microresonator, with surface roughness considerably smaller than that of the microdisk was formed [86]. The schematics of the CO_2 laser reflow setup can be seen in Figure 4.5. See Figure 4.6 for SEM images of the fabricated microdisk and microtoroid.

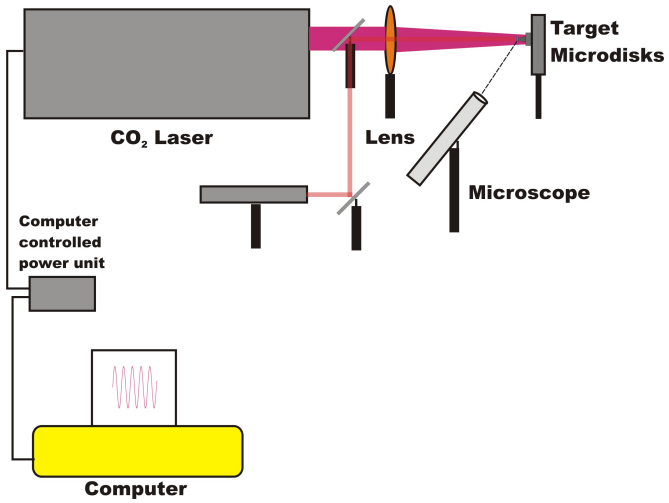

Figure 4.5: Schematics of the CO_2 laser reflow setup.

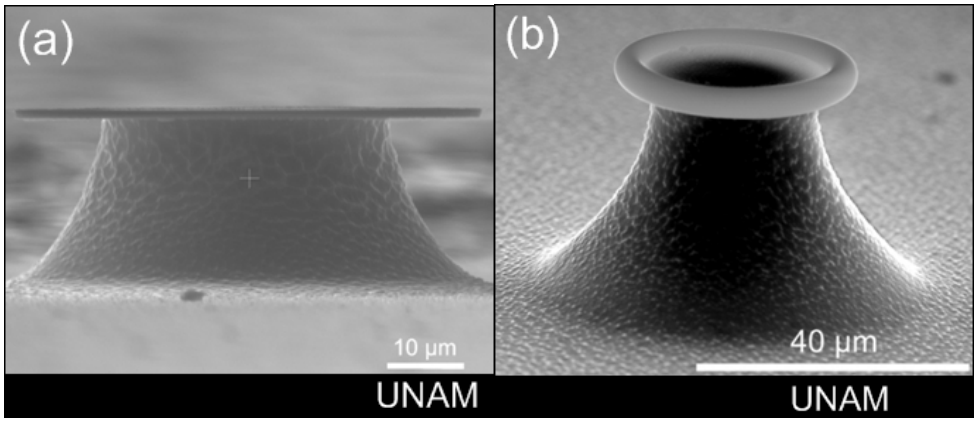

Figure 4.6: (a) SEM image of the obtained microdisk. (b) SEM image of the microdisk shown in (a) after being reflown with CO_2 laser.

The surface roughness at the center and at the rim of the microtoroid was measured using PSIA Atomic Force Microscope (AFM). The average surface

roughness at the center of the toroid is ∼12 nm whereas the average surface roughness on the rim of the toroid is ∼0.2 nm, substantiating the effect of reflow process as demonstrated in Figure 4.7.

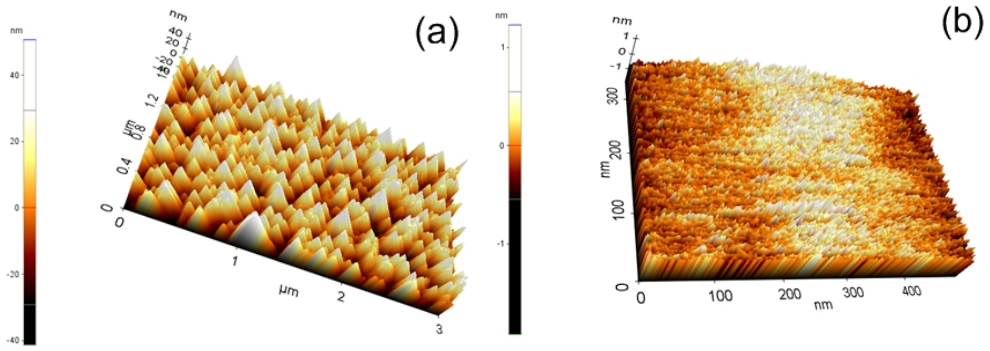

Figure 4.7: (a) Surface roughness measured at the central region of the microtoroid. (b) Surface roughness measured at the rim of the microtoroid.

An interesting situation occurs when the diameter of the microdisk and the supporting silicon pillar, together with the thickness of the oxide layer, i.e. the microdisk are adjusted so that some portion of the melted silica microstructure cannot be supported by the narrow silicon pillar underneath and pours down on to the substrate where the remaining part forms a microsphere by surface tension. The SEM images of such a microdisk before and after reflow were given in Figure 4.8.

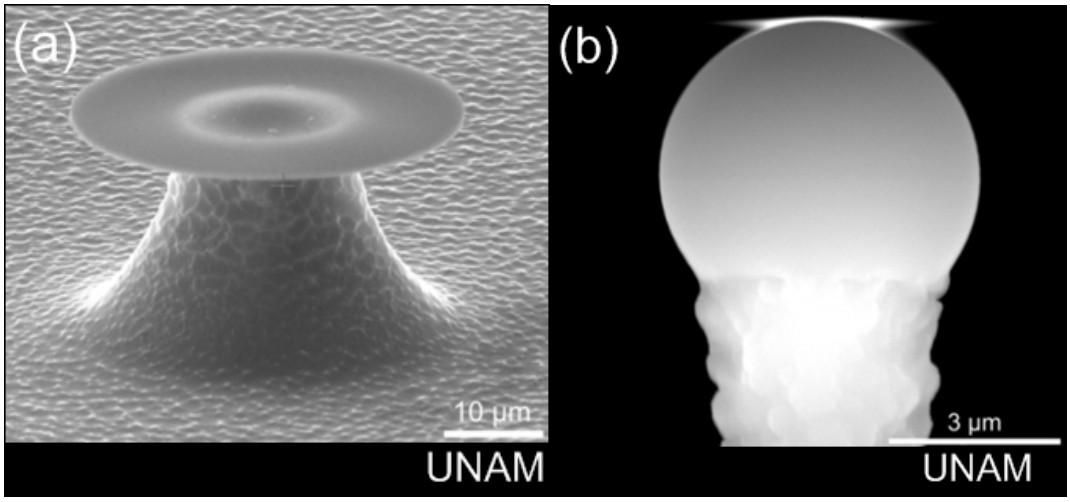

Figure 4.8: (a) SEM image of the microdisk before the reflow process. (b) Same disk after the reflow process. Note the transformed geometry in this case is not toroid; instead it is a sphere after reflow.

For observation of laser action from a toroidal microresonator, the cavities were spin coated with DOO-PPV polymer. For this purpose, the polymer was dissolved in toluene at 10 mg/ml concentration and spun on to microstructures with a rate of 1000 rpm. The thickness of the polymer on the microtoroid is $\sim$1 μm. After spin coating, samples were kept at 90°C under rough vacuum conditions for 6 hours to ensure cleanliness and smoothness of the polymer layer. The AFM measurements yielded an average surface roughness of $\sim$1 nm for this microstructure, Figure 4.9.

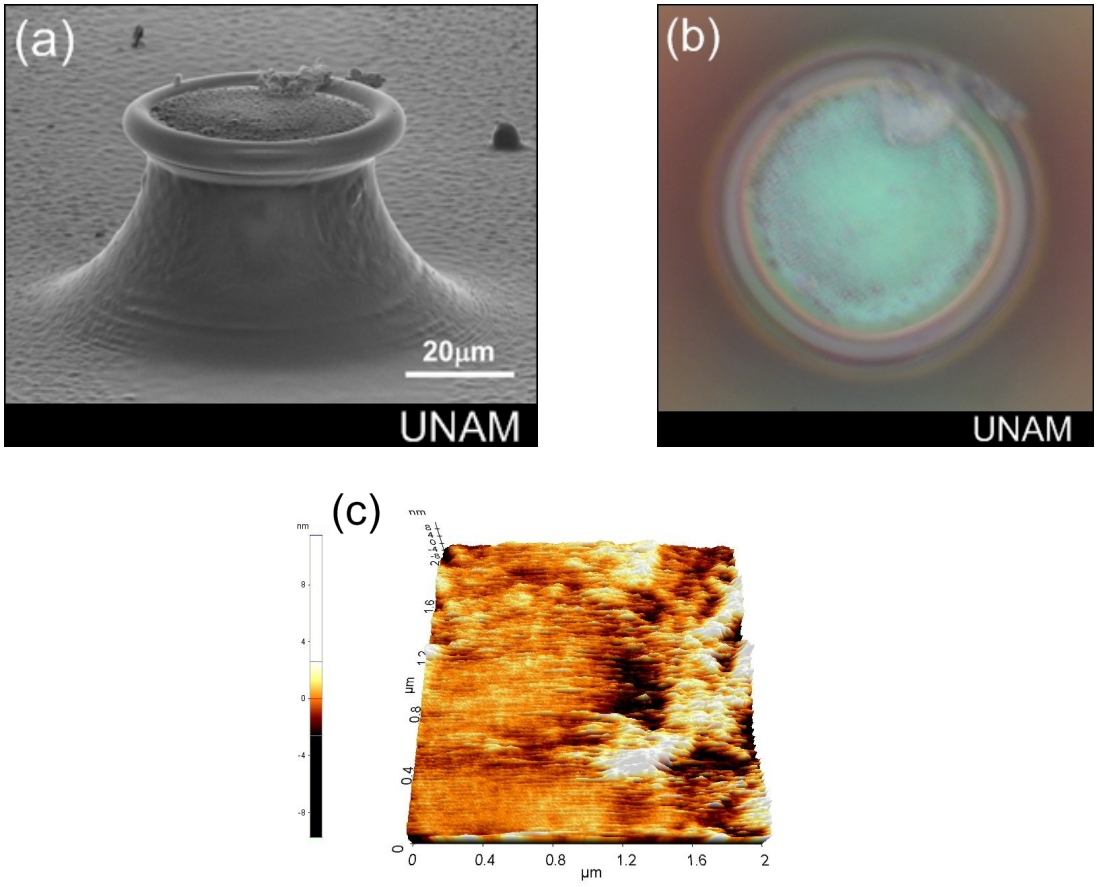

Figure 4.9: (a) SEM image of the DOO-PPV coated microtoroid. (b) Optical microscope image of the of the very same microcavity in (a). (c) AFM measurement performed on the same microstructure.

4.5 Experimental Setup

Polymer coated microtoroid was excited with OPA-800C system, which was described in full detail in Chapter 3. The excitation wavelength was set to 520 nm by sum frequency generation. After light exits the OPA, it was guided by a mirror, M1 to a neutral density filter followed by an iris, which are used to adjust the intensity of light. Then by mirror M2 and a cylindrical lens, light was focused on to the microtoroid from which the laser action was to be observed. Emission from the microtoroid laser was collected by a multi mode fiber and guided to

DK-480 spectrometer. The difference between using DK-480 as a monochromator or a spectrometer is that in the case of spectrometer, a CCD camera is placed at the exit of DK-480 where the spatial distribution of wavelengths is recorded.

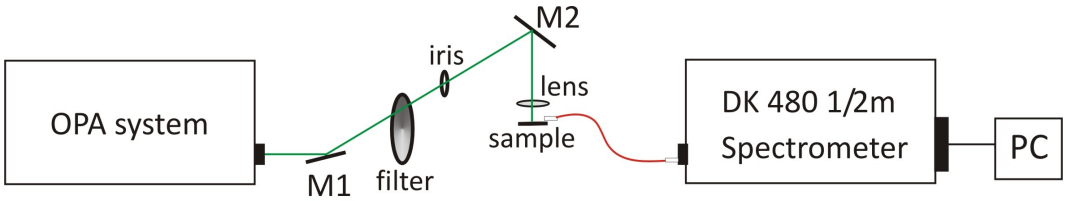

Figure 4.10: The schematics of the experimental setup for observing laser action from DOO-PPV coated microtoroid.

4.6 Measurements and Results

Polymer coated microtoroid was excited using free space excitation at 520 nm wavelength with various power levels. Laser emission peaks with ∼0.3 nm FWHM were observed after a certain threshold was attained.

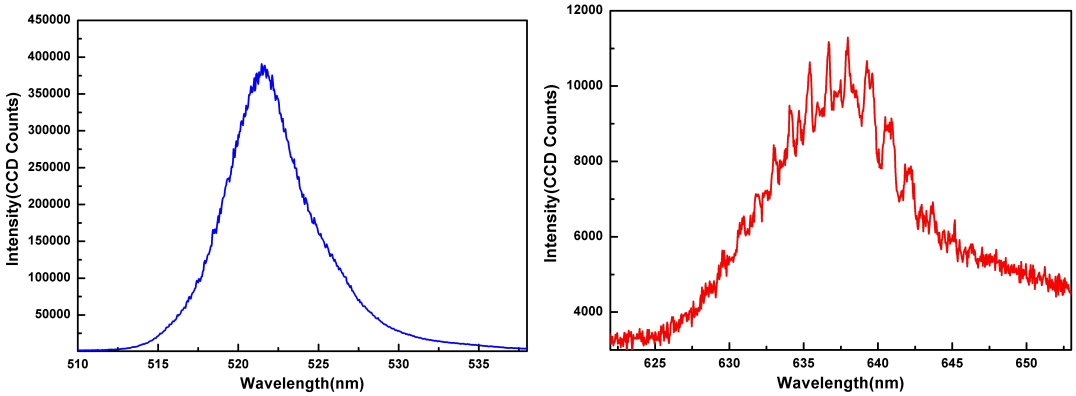

Figure 4.11: (a) OPA excitation. (b) Emission spectrum observed from DOO-PPV coated microtoroid laser.

In Figure 4.11b, the emission spectrum observed from polymer coated microcavity was recorded at 0.25 mW average pump power level. After cylindrical

lens, the beam falls down to a ∼4.5 mm by ∼0.55 mm area where a 56.5 μm diameter toroid microlaser was located. Therefore, the average power of light falling onto microtoroid is approximately:

$$P_{av} = \frac{0.25 \times \pi \times (28.25 \times 10^{-6})^2}{4.5 \times 10^{-3} \times 0.55 \times 10^{-3}} mW = 253.25nW \tag{4.1}$$

Since the repetition rate of the pump laser was 1 kHz, the excitation energy per pulse would be E_{pulse}=P_{av}/rep.rate=253.25 pJ/pulse. In Figure 4.12, the emission intensity of toroid microlaser is given in units of CCD counts as a function of the excitation energy level. From this graph, we can see that there is a threshold behavior at ∼200 pJ/pulse.

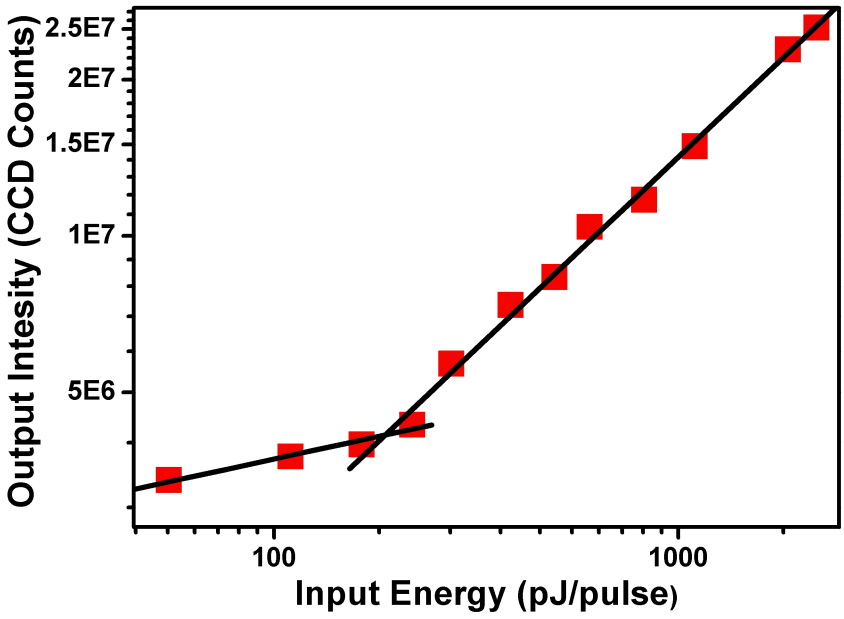

Figure 4.12: The lasing emission intensity from microtoroid vs the input pulse energy.

In Figure 4.13, lasing spectrum at 440 pJ/pulse excitation energy and its Fast Fourier Transform (FFT) is provided.

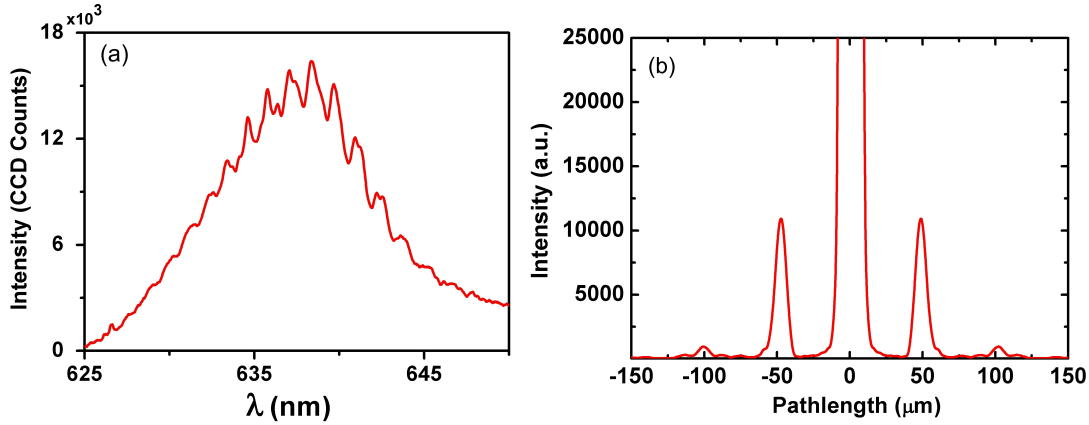

Figure 4.13: (a) The lasing spectrum obtained at 440 pJ/pulse excitation energy. (b) The FFT of the lasing spectrum shown in (a).

FFT is a useful tool in relating the location of the observed peaks to cavity size. For example, the Fourier Transform of the transmitted intensity for a Fabry-Perot cavity can be written as [87]:

$$I(u) = |1 - Re^{2i\phi}|^2 \sum_{m=0}^{\infty} \sum_{l=0}^{\infty} \frac{R^{l+m} e^{(-2i\phi(l-m))}}{kd(l+m+1) + i(\pi u + nd(l-m))} \tag{4.2}$$

where u is the optical pathlength; k is the extinction coefficient; d is the mirror separation; R is the mirror reflectivity; ϕ is the phase change upon reflection; l and m are integers. In the case of low absorption where $k \sim 0$, the peaks are located where the imaginary part of the denominator becomes zero:

$$u = \frac{nd}{\pi}(l-m) = \frac{nd}{\pi}N \tag{4.3}$$

where N is the combined integer of *(l-m)*. The equations for Fabry-Perot cavity work well for whispering gallery mode cavities, too. Therefore, when the mirror separation, d of the Fabry-Perot cavity is replaced by $\pi \times D/2$ with D being the cavity diameter, the mode spacing, $\Delta\lambda$ is:

$$\Delta\lambda = \frac{\lambda^2}{2nd} = \frac{\lambda^2}{\pi n D} \tag{4.4}$$

In addition, the Fourier components in the FFT of laser emission spectrum, are separated by distance of $nD/2$ where n is the effective refractive index of the

medium, and D is the diameter of microcavity. In our case, the peak separation between Fourier components is 50.5 μm. The major diameter of microtoroid was measured to be $\sim$56.5 μm from the optical microscope images. When the effective refractive index of the medium is calculated using this value, n_{eff} $\sim$1.787 is found. The refractive index of DOO-PPV, as seen from ellipsometer data, is 1.790 at 637 nm wavelength. Hence the effective refractive index of the active medium is very close to refractive index of the bulk material. This indicates, light is mostly confined to DOO-PPV layer on the microtoroid, suggesting that laser resonances are whispering gallery type, which is ensured by total internal reflection condition.

To sum up, lasing behavior from DOO-PPV coated microtoroid was observed with a threshold level of $\sim$200 pJ/pulse. This is the lowest value observed for a microtoroidal cavity as far as free space excitation is considered. This result can lead to ultralow threshold lasers, without using difficult light coupling mechanisms [29].

Chapter 5

CONCLUSION and FUTURE WORKS

The spectral broadening inside a nanostructured As_2Se_3 core and PES cladding fiber was investigated. For this purpose, the spectra from two different chalcogenide fiber lengths and spectra from PES fibers were compared.

We have observed considerable spectral broadening at ∼1500 nm in nanostructured chalcogenide fibers, whereas the same effect was not strong at ∼2000 nm, as we anticipated. The reason for such a behavior is attributed to the fact that PES is not an efficient cladding material in the IR region, due to its strong absorbance leading to significant attenuation of the signal.

In addition, the total dispersion of fiber is still too high in the IR region, preventing a substantial broadening. Therefore this property needs to be tailored if a broadband continuum source is desired. This aim can be achieved either by a new fiber design where the waveguide dispersion is engineered to obtain the desired features, or by tapering the used fiber down to the extent that nonlinear interactions are enhanced and total chromatic dispersion is reduced. Moreover

it is always possible to utilize both approaches together to acquire the optimum characteristics.

Apart from fiber structure, nonlinear interactions were also investigated numerically in a toroid microresonator geometry, where we observed frequency comb generation even with very small peak power levels. Therefore as for the future work, it is important to observe such an effect experimentally in this type of geometry using chalcogenide materials.

Laser action was observed from DOO-PPV coated microtoroid with free space excitation. The recorded threshold value was the lowest for a microtoroid as far as free space excitation is considered. This result is important to show that when high quantum efficiency of polymers is combined with the ultra high quality factor of microtoroid, low threshold lasing can be achieved while avoiding the difficulties of evanescent wave coupling mechanisms.

In the future work, different gain media emitting in various wavelengths, with high quantum efficiency can be utilized to observe laser action in a wide range of spectrum, with lower threshold energy. Moreover it is always possible to reflow different geometries to obtain toroid like structures; therefore a new class of resonators with ultrahigh quality factor retaining different shapes such as ellipse, spiral and stadium can be fabricated; thus many different physical concepts which can not occur in a cylindrically symmetric toroid such as directional laser emission or chaotic laser modes can be studied much efficiently than before.

Bibliography

[1] G. S. He, T. C. Lin, and P. N. Prasad, "New technique for degenerate two-photon absorption spectral measurements using femtosecond continuum generation," *Optics Express*, vol. 10, no. 13, pp. 566–574, 2002.

[2] S. T. Sanders, "Wavelength-agile fiber laser using group-velocity dispersion of pulsed super-continua and application to broadband absorption spectroscopy," *Appl. Phys. B-Lasers Opt.*, vol. 75, pp. 799–802, 2002.

[3] S. A. Diddams, D. J. Jones, J. Ye, S. T. Cundiff, J. L. Hall, J. K. Ranka, R. S. Windeler, R. Holzwarth, T. Udem, and T. Hänsch, "Direct link between microwave and optical frequencies with a 300 thz femtosecond laser comb," *Physical Review Letters*, vol. 84, no. 22, pp. 5102–5105, 2000.

[4] Y. M. Wang, Y. H. Zhao, J. S. Nelson, Z. P. Chen, and R. S. Windeler, "Ultrahigh-resolution optical coherence tomography by broadband continuum generation from a photonic crystal fiber," *Optics Letters*, vol. 28, no. 3, pp. 182–184, 2003.

[5] D. L. Marks, A. L. Oldenburg, J. J. Reynolds, and S. A. Boppart, "Study of an ultrahigh-numerical-aperture fiber continuum generation source for optical coherence tomography," *Optics Letters*, vol. 27, no. 22, pp. 2010–2012, 2002.

[6] F. Futami and K. Kikuchi, "Low-noise multiwavelength transmitter using spectrum-sliced supercontinuum generated from a normal group-velocity

dispersion fiber," *IEEE Photonics Tech. Lett.*, vol. 13, no. 1, pp. 73–75, 2001.

[7] L. Boivin, S. Taccheo, C. R. Doerr, P. Schiffer, L. W. Stulz, R. Monnard, and W. Lin, "400 Gbit/s transmission over 544 km from spectrum-sliced supercontinuum source," *Electron. Lett.*, vol. 36, no. 4, pp. 335–336, 2000.

[8] R. Alfano and S. Shapiro, "Observation of self-phase modulation and small-scale filaments in crystals and glasses," *Physical Review Letters*, vol. 24, no. 11, pp. 592–594, 1970.

[9] R. Alfano and S. Shapiro, "Emission in the region 4000 to 7000 A° via four-photon coupling in glass," *Physical Review Letters*, vol. 24, no. 11, pp. 584–587, 1970.

[10] R. A. J. M. P.B. Corkum, P.P.Ho, "Generation of infrared supercontinuum covering 3-14 μm in dielectrics and semiconductors," *Optics Letters*, vol. 10, no. 12, pp. 624–626, 1985.

[11] P. P. Ho, Q. X. Li, T. Jimbo, Y. L. Ku, and R. R. Alfano, "Supercontinuum pulse generation and propagation in a liquid carbontetrachloride," *Applied Optics*, vol. 26, no. 14, pp. 2700–2702, 1987.

[12] P. Corkum, C. Rolland, and T. Srinivasan-Rao, "Supercontinuum generation in gases," *Physical Review Letters*, vol. 57, no. 18, pp. 2268–2271, 1985.

[13] S. G. Leon-Saval, T. A. Birks, W. J. Wadsworth, and P. S. Russell, "Supercontinuum generation in submicron fibre waveguides," *Optics Express*, vol. 12, no. 13, pp. 2864–2869, 2004.

[14] J. Ranka, R. Windeler, and A. Stentz, "Visible continuum generation in air-silica microstructure optical fibers with anomalous dispersion at 800 nm," *Optics Letters*, vol. 25, no. 1, pp. 25–27, 2000.

[15] D.-I. Yeom, E. C. Mägi, M. R. E. Lamont, M. A. F. Roelens, L. Fu, and B. J. Eggleton, "Low-threshold supercontinuum generation in highly nonlinear chalcogenide nanowires," *Optics Letters*, vol. 33, no. 7, pp. 660–662, 2008.

[16] J. Dudley, G. Genty, and S. Coen, "Supercontinuum generation in photonic crystal fiber," *Rev. of Modern Physics*, vol. 78, pp. 1135–1184, 2006.

[17] H. Rokhsari and K. Vahala, "Observation of Kerr nonlinearity in microcavities at room temperature," *Optics Letters*, vol. 30, no. 4, pp. 427–429, 2005.

[18] T. Carmon and K. Vahala, "Visible continuous emission from a silica microphotonic device by third-harmonic generation," *Nature Physics*, vol. 3, pp. 430–435, 2007.

[19] A. A. Savchenkov, V. S. Ilchenko, A. B. Matsko, and L. Maleki, "Tunable filter based on whispering gallery modes," *Elelctron. Lett.*, vol. 39, no. 4, pp. 389–391, 2003.

[20] H. Latifi, A. Biswas, R. L. Armstrong, and R. G. Pinnick, "Lasing and stimulated Raman scattering in spherical droplets -time, irradiance, and wavelength dependence," *Appl.Opt.*, vol. 29, no. 36, pp. 5387–5392, 1990.

[21] B. Min, S. Kim, K. Okamoto, L. Yang, A.Scherer, H. Atwater, and K. Vahala, "Ultralow threshold on-chip microcavity nanocrystal quantum dot lasers," *Applied Physics Letters*, vol. 89, p. 191124, 2006.

[22] A. M. Armani, R. P. Kulkarni, S. E. Fraser, R. C. Flagan, and K. J. Vahala, "Label-free single-molecule detection with optical microcavities," *Science*, vol. 317, pp. 783–787, 2007.

[23] B. Dayan, A. S. Parkins, T. Aoki, E. P. Ostby, K. J. Vahala, and H. J. Kimble, "A photon turnstile dynamically regulated by one atom," *Science*, vol. 319, pp. 1062–1065, 2008.

[24] D. W. Vernooy, A. Furusawa, N. P. Georgiades, V. S. Ilchenko, and H. J. Kimble, "Cavity QED with high-Q whispering gallery modes," *Phys. Rev. A*, vol. 57, no. 4, pp. R2293–R2296, 1998.

[25] D. W. Vernooy, V. S. Ilchenko, H. Mabuchi, E. W. Streed, and H. J. Kimble, "High-Q measurements of fused-silica microspheres in the near infrared," *Optics Letters*, vol. 23, no. 4, pp. 247–249, 1998.

[26] L. Collot, V. Lefevre-Seguin, M. Brune, J. Raimond, and S. Haroche, "Very high-Q whispering gallery mode resonances observed on fused-silica microspheres," *Europhys. Lett*, vol. 23, no. 5, pp. 327–334, 1993.

[27] D. Armani, T. Kippenberg, S. Spillane, and K. Vahala, "Ultra-high-Q toroid microcavity on a chip," *Nature*, vol. 421, no. 6926, pp. 925–928, 2003.

[28] "D. Akbulut, A. Tülek and M. Bayındır, in preparation."

[29] "A. Tülek, D. Akbulut and M. Bayındır, in preparation."

[30] C. R. Pollock, *Fundamentals of optoelectronics*. Irwin.

[31] G. Agrawal, *Nonlinear Fiber Optics*. Academic Press.

[32] R. Boyd, *Nonlinear Optics*. Academic Press.

[33] J.-K. Kim, *Investigation of High-Nonlinearity Glass Fibers for Potential Applications in Ultrafast Nonlinear Fiber Devices*. PhD thesis, Virginia Polytechnic Institute and State University, 2005.

[34] D. Alasia, *Advanced Trends in Nonlinear Optics Applied to Distributed Optical-Fibre Sensors*. PhD thesis, Ecole Polytechnique Federal de Lausanne, 2006.

[35] A. Tulek, *Laser Action From Microcavities of Pi-Conjugated Polymers*. PhD thesis, The University of Utah, 2008.

[36] M. Csele, *Fundamentals of light sources and lasers*. Wiley-Interscience.

[37] "Encyclopedia of laser physics and technology, http://www.rp-photonics.com."

[38] K. Vahala, "Optical microcavities," *Nature*, vol. 424, no. 6950, pp. 839–846, 2003.

[39] B. E. Little, J.-P. Laine, and H. A. Haus, "Analytic theory of coupling from tapered fibers and half-blocks into microsphere resonators," *J. Light. Tech.*, vol. 17, no. 4, pp. 704–715, 1999.

[40] K. Vahala, *Optical Microcavities*. World Scientific.

[41] T. Kippenberg, *Nonlinear Optics in Ultra-High-Q Whispering-Gallery Optical Microcavities*. PhD thesis, California Institute of Technology, 2004.

[42] S. Spillane, *Fiber-coupled ultra-high-Q microresonators for nonlinear and quantum optics*. PhD thesis, California Institute of Technology, 2004.

[43] H. L. M. Lehtonen, G. Genty, "Absorption and transmission spectral measurement of fiber-optic components using supercontinuum radiation," *Appl. Phys. B*, vol. 81, pp. 231–234, 2005.

[44] S. L. Chin, S. Petit, F. Borne, and K. Miyazaki, "The white light supercontinuum is indeed an ultrafast white light laser," *Jpn. J. Appl. Phys. Part 2 - Lett.*, vol. 38, pp. L126–L128, 1999.

[45] K. Hansen and R. Kristiansen, "Supercontinuum generation in photonic crystal fibers," *Application Note, Crystal-Fibre*.

[46] C. Lin and R. Stolen, "New nanosecond continuum for excited state spectroscopy," *Applied Physics Letters*, vol. 28, no. 4, pp. 216–218, 1976.

[47] G. Genty, *Supercontinuum generation in microstructured optical fibers and novel optical measurement techniques*. PhD thesis, Helsinki University of Technology, 2004.

[48] P. Kaiser, E. A. J. Marcatili, and S. E. Miller, "A new optical fiber," *Bell Syst. Tech. J*, vol. 52, pp. 265–269, 1973.

[49] J. C. Knight, T. A. Birks, P. S. J. Russell, and D. M. Atkin, "All-silica single-mode optical fiber with photonic crystal cladding," *Optics Letters*, vol. 21, no. 19, pp. 1547–1549, 1996.

[50] T. A. Birks, J. C. Knight, and P. S. J. Russell, "Endlessly single-mode photonic crystal fiber," *Optics Letters*, vol. 22, no. 13, pp. 961–963, 1997.

[51] G. Bouwmans, F. Luan, J. C. Knight, P. S. J. Russell, L. Farr, B. J. Mangan, and H. Sabert, "Properties of a hollow-core photonic bandgap fiber at 850 nm wavelength," *Optics Letters*, vol. 11, no. 14, pp. 1613–1620, 2003.

[52] T. Birks, W. Wadsworth, and P. Russell, "Supercontinuum generation in tapered fibers," *Optics Letters*, vol. 25, no. 19, pp. 1415–1417, 2000.

[53] S. Leon-Saval, T. Birks, W. Wadsworth, P. Russell, and M. Mason, "Supercontinuum generation in submicron fiber waveguides," *Optics Express*, vol. 12, no. 13, pp. 2864–2869, 2004.

[54] R. R. Gattass, G. T. Svacha, L. Tong, and E. Mazur, "Supercontinuum generation in submicrometer diameter silica fibers," *Optics Express*, vol. 14, no. 20, pp. 9408–9414, 2006.

[55] J. Y. Y. Leong, P. Petropoulos, J. H. V. Price, H. Ebendorff-Heidepriem, S. Asimakis, R. C. Moore, K. E. Frampton, V. Finazzi, X. Feng, T. M. Monro, and D. J. Richardson, "High-nonlinearity dispersion-shifted lead-silicate holey fibers for efficient 1 μm pumped supercontinuum generation," *Journal of Lightwave Technology*, vol. 24, no. 1, pp. 183–190, 2006.

[56] G. Brambilla, F. Koizumi, V. Finazzi, and D. Richardson, "Supercontinuum generation in tapered bismuth silicate fibers," *Electronics Letters*, vol. 41, no. 14, pp. 795–797, 2005.

[57] I.-W. Hsieh, X. Chen, X. Liu, J. I. Dadap, N. C. Panoiu, C.-Y. Chou, F. Xia, W. M. Green, Y. A. Vlasov, and J. Richard M. Osgood, "Supercontinuum generation in silicon photonic wires," *Optics Express*, vol. 15, no. 23, pp. 15242–15249, 2007.

[58] N. D. Psaila, R. R. Thomson, H. T. Bookey, S. Shen, N. Chiodo, R. Osellame, G. Cerullo, A. Jha, and A. K. Kar, "Supercontinuum generation in an ultrafast laser inscribed chalcogenide glass waveguide," *Optics Express*, vol. 15, no. 24, pp. 15776–15781, 2007.

[59] M. R. Lamont, B. Luther-Davies, D.-Y. Choi, S. Madden, and B. J. Eggleton, "Supercontinuum generation in dispersion engineered highly nonlinear ($\gamma = 10/\mathrm{w/m}$) as_2s_3 chalcogenide planar waveguide," *Optics Express*, vol. 16, no. 19, pp. 14938–14944, 2008.

[60] M. Bayindir, A. Abouraddy, O. Shapira, J. Viens, D. Saygin-Hinczewski, F. Sorin, J. Arnold, J. Joannopoulos, and Y. Fink, "Kilometer-long ordered nanophotonic devices by preform-to-fiber fabrication," *IEEE Journal of Selected Topics in Quantum Electronics*, vol. 12, no. 6, pp. 1202–1213, 2006.

[61] Spectra Physics, *Millennia Pro s-Series User's Manual*.

[62] Spectra Physics, *Tsunami User's Manual*.

[63] Spectra Physics, *Empower User's Manual*.

[64] Spectra Physics, *Spitfire Pro User's Manual*.

[65] Spectra Physics, *OPA-800C User's Manual*.

[66] Spectral Products, *Digikrom DK 480 1/2 Meter Monochromator/Spectrograph user manual*.

[67] T. Baba, P. Fujita, A. Sakai, M. Kihara, and R. Watanabe, "Lasing characteristics of GaInAsP-InP strained quantum-well microdisk injection lasers

with diameter of 2-10 μm," *IEEE Photon. Tech. Lett.*, vol. 9, no. 7, pp. 878–880, 1997.

[68] A. Belarouci, K. B. Hill, Y. Liu, Y. Xiong, T. Chang, and A. E. Craig, "Design and modeling of waveguide-coupled microring resonator," *Journal of Luminescence*, vol. 94-95, pp. 35–38, 2001.

[69] A. Kiraz, A. Kurt, M. A. Dündar, and A. L. Demirel, "Simple largely tunable optical microcavity," *Appl. Phys. Lett.*, vol. 89, no. 081118, 2006.

[70] M. L. Gorodetsky, A. A. Savchenkov, and V. S. Ilchenko, "Ultimate Q of optical microsphere resonators," *Optics Letters*, vol. 21, no. 7, pp. 453–455, 1996.

[71] A. B. Matsko and V. S. Ilchenko, "Optical resonators with whispering-gallery modes-part I: Basics," *IEEE Journal of Selected Topics in Quantum Electronics*, vol. 12, no. 1, pp. 3–14, 2006.

[72] P. D. Haye, A. Schliesser, O. Arcizet, T. Wilken, R. Holzwarth, and T. J. Kippenberg, "Optical frequency comb generation from a monolithic microresonator," *Nature*, vol. 450, pp. 1214–1217, 2007.

[73] RSoft Photonics Suite, *FullWAVE^{TM} 6.0 User Guide*.

[74] V. S. Ilchenko, A. A. Savchenkov, A. B. Matsko, and L. Maleki, "Nonlinear optics and crystalline whispering gallery mode cavities," *Physical Review Letters*, vol. 92, no. 4, p. 043903, 2004.

[75] V. Sandoghdar, F. Treussart, J. Hare, V. Lefevre-Seguin, J. M. Raimond, and S. Haroche, "Very low threshold whispering-gallery-mode microsphere laser," *Phys.Rev.A*, vol. 54, no. 3, pp. R1777–R1780, 1996.

[76] T. J. Kippenberg, S. M. Spillane, and K. J. Vahala, "Demonstration of ultra-high-Q small mode volume toroid microcavities on a chip," *Applied Physics Letters*, vol. 85, no. 25, pp. 6113–6115, 2004.

[77] T. Aoki, B. Dayan, E. Wilcut, W. P. Bowen, A. S. Parkins, T. J. Kippenberg, K. J. Vahala, and H. J. Kimble, "Observation of strong coupling between one atom and a monolithic microresonator," *Nature*, vol. 443, pp. 671–674, 2006.

[78] A. M. Armani and K. J. Vahala, "Heavy water detection using ultra-high-Q microcavities," *Optics Letters*, vol. 31, no. 12, pp. 1896–1898, 2006.

[79] B. Min, T. Kippenberg, L. Yang, and K. Vahala, "Erbium implanted high-Q silica toroidal microcavity laser on a silicon chip," *Physical Review A*, vol. 70, p. 033803, 2004.

[80] E. Ostby, L. Yang, and K. Vahala, "Ultralow-threshold Yb^{3+}:Sio_2 glass laser fabricated by the solgel process," *Optics Letters*, vol. 32, no. 18, pp. 2650–2652, 2007.

[81] U. Koldemir, "Conjugated polymers based on polyfluorene derivatives and polypyrrole," Master's thesis, Bilkent University, 2007.

[82] S. V. Frolov, M. Shkunov, A. Fujii, K. Yoshino, and Z. V. Vardeny, "Lasing and stimulated emission in π-conjugated polymers," *IEEE J. Quantum Electron.*, vol. 36, no. 1, pp. 2–11, 2000.

[83] M. Cai, O. Painter, P. Sercel, and K. J. Vahala, "Fiber-coupled microsphere laser," *Optics Letters*, vol. 25, no. 19, pp. 1430–1432, 2000.

[84] N. Dubreuil, J. C. Knight, D. K. Leventhal, V. Sandoghdar, J. Hare, and V. Lefévre, "Eroded monomode optical fiber for whispering-gallery mode excitation in fused-silica microspheres," *Optics Letters*, vol. 20, no. 8, pp. 813–815, 1995.

[85] Clariant, *AZ 5214 E Product Data Sheet*.

[86] D. Armani, *Ultra-High-Q Planar Microcavities and Applications*. PhD thesis, California Institute of Technology, 2005.

[87] D. Hofstetter and R. L. Thornton, "Measurement of optical cavity properties in semiconductor lasers by fourier analysis of the emission spectrum," *IEEE Journal of Quantum Electronics*, vol. 34, no. 10, pp. 1914–1923, 1998.